A Model for an Optical Ring Microresonator towards Nanoparticle Detection

A thesis submitted to the
Graduate School of Natural and Applied Sciences

by

Faruk AHMETI

in partial fulfillment for the
degree of Master of Science

in

Electronics and Computer Engineering

İSTANBUL
ŞEHİR
UNIVERSITY

This is to certify that we have read this thesis and that in our opinion it is fully adequate, in scope and quality, as a thesis for the degree of Master of Science in Electronics and Computer Engineering.

APPROVED BY:

Prof. Dr. Kaşif Teker
(Thesis Advisor)

Assoc. Prof. Dr. Tansal Güçlüioğlu

Asst. Prof. Dr.Ali Çakmak

This is to confirm that this thesis complies with all the standards set by the Graduate School of Natural and Applied Sciences of İstanbul Şehir University:

DATE OF APPROVAL: 4 August 2017.

SEAL/SIGNATURE:

Declaration of Authorship

I, Faruk AHMETI, declare that this thesis titled, 'A Model for an Optical Ring Microresonator towards Nanoparticle Detection ' and the work presented in it are my own. I confirm that:

- This work was done wholly or mainly while in candidature for a research degree at this University.

- Where any part of this thesis has previously been submitted for a degree or any other qualification at this University or any other institution, this has been clearly stated.

- Where I have consulted the published work of others, this is always clearly attributed.

- Where I have quoted from the work of others, the source is always given. With the exception of such quotations, this thesis is entirely my own work.

- I have acknowledged all main sources of help.

- Where the thesis is based on work done by myself jointly with others, I have made clear exactly what was done by others and what I have contributed myself.

Signed:

Date: 04.08.2017

A Model for an Optical Ring Microresonator towards Nanoparticle Detection

Faruk AHMETI

Abstract

High-Q optical resonators are very prominent bio-sensing technologies that confines light inside a microsize system. Due to their small size and dielectric fabrication materials, these systems can be integrated cost-effectively on integrated chips along with other optical and electrical components. Measurement of the resonance shift proceeded by the transmission spectrum enables observation of binding events in real time, and can also be used to characterize particle size and type. Combination of small size and high Q factor empowers these devices with excellent detection capability. In this thesis, an optical microring resonator has been developed through a multiphysics model using finite element method to solve the relevant equations. All the platform was built in COMSOL Multyphisics software tool. The general framework of this sensor is based on a laser light source, a straight-shape waveguide, a ring-based waveguide, and a photodector at the end of the straight waveguide. A communication laser was used to generate the light at a wavelength of 1.55 μm.

In this thesis, it is important to achieve single particle detection inside an aqueous environment since most of the clinical samples are water based. The exact position of the resonance wavelength is located and the transmission spectrum is recorded. A linear correlation between the red shift in the resonance wavelength and increase in the radius of the microring is observed. When the ring radius was increased, there was a resonance shift in the wavelength towards higher values. It was also found that a resonance shift for a value as small as 10 nm could be detected. The interaction between the resonator and nanoparticles is implemented in a unique way. This implementation is performed by modeling nanoparticles by a layer around the ring and then changing its thickness with the corresponding refraction index of analyzed nanoparticle. This will affect the resonance when it is compared to the resonator response without the layer. The resonance shift should be in a linear trend in order to be able to use as biodetection sensor. The interaction between a single particle and the sensor itself determine the sensing capability within a rapid time. The detection of a mimicked titanium dioxide nanoparticle as well as protein biomolecule with an effective size starting from around 10 nm in diameter has been reported.

Keywords: Optical Resonators, Resonance Shift, Photonic, Biosensing

Nano Parçacıkların Tespit Edilmesinde Kullanılan Optik Halka Mikro Rezonator için Bir Model

Faruk AHMETI

Öz

Optik rezonatorler temel yapıtaşları olarak fotonlu araçları ve lazerler, yukselticiler, optik suzgeçler, çok duzeyli optik birleştiriciler, mantık geçitleri, anahtarlar ve sensorleri içeren uygulamalar alanında onemli bir potansiyele sahiptir. Bir mikrorezonator ışığı toplam iç yansıma ile sınırlandıran mikron boyutta dairesel geometri (mikrodisk, mikrokure, mikrotor ve mikrohalka) ile tanımlanır. Klasik tabloda, dairenin çevresinin etrafındaki dairesel ışığın uzunluğunun yolu dalga boyunun tam katına denk geldiğinde optik rezonanslar rezonatore birleştirilir. Halka rezonatorde, bu rezonator iletim spektrumlarındaki keskin bir duşuş olarak tanımlanır, genel olarak tonu ayarlanabilir lazer ışınlarını rezonatorun yakınlarına yerleştirilmiş konikleştirilmiş optik fiber ile rezonatore ulaştırarak elde edilir. Rezonans duşuşleri, iletim spektrumu lazer dalga boyları uzerinde gezinirken olçulerek gozlemlenebilir. Lazerin dalga boyları halkanın rezonans dalga boyları ile eşleştiğinde, ışık optik fiberden mikrohalkaya birleşir, sonuç olarak doğru dalga kılavuzunun çıktısı olarak iletim spektrumunun yoğunluğunda duşuş olarak gozlemlenir.

Bu çalışmada, mikrohalka temelli bir rezonator kullanıldı ve aşırı hassas biyomolekul ve nano parçacık tespiti için bu rezonatorun multifizik olçulebilir element modeli geliştirildi. Bu model COMSOL Multiphysics v5.2 kullanılarak tasarlandı. 1.55 μm dalga boyundaki dalga kılavuzunun giriş duğumunde giriş lazer ışığı kullandık ve yayılan ışık çıkış duğumunde gozlemlendi. Bu sureç boyunca, iletim spektrumunu kaydettik ve mikrohalkanın rezonans dalga boyunun tam konumunu belirledik. Halkanın yarıçapını arttırdığımızda, rezonans dalga boyları daha yuksek dalga boylarına (kızıla kayma) doğru kaydı. Mikrohalkanın yarıçapı ile rezonans dalga boylarındaki kızıla kayma arasında doğrusal bir ilişki olduğunu gorduk. Buna ek olarak, mikrohalkanın yarıçapındaki değişiklikler 10 nm kadar bile kuçuk olsa da bu değişimi gorebildiğimizi fark ettik.

Anahtar Sözcükler: Optik Halka Rezonatorleri, Rezonans Kayması, Fotonik

To my parents . . .

Acknowledgments

Firstly, I would like to thank the Almighty God for all the blessings to me and my family.

I would like to express my sincere gratitude to my thesis advisor Prof. Kaşif Teker for the useful comments, excellent guidance, and his support for my research and thesis completion. I have learned many things since I became Dr. Teker's student. He spent very much of his valuable time instructing me on many academics and life guides.

I would like to thank Prof. Dr Tansal Güçlüoğlu and Prof. Dr Ali Çakmak for taking out time to be a part of my thesis committee.

Special thanks are given to Department of Electronics and Computer Engineering.

Also, I would like to thank Prof. Hakan Doğan that was very supportive to me. For his valuable time that spent with me.

During the study period, many friends were really helpful and in a way or another they colored my life. I have to acknowledge all my colleagues of the department and MEMS team. I would like to specify Hassan Gibaly, Rashad Kasim and Ramy Rady. A special thanks to my close friend and roommate Egzonis Hajdari.

Last but not the least, I would like to express my very deep gratitude to my parents, my father Ahmet Ahmeti, my mother Mevlude Havolli Ahmeti, my two sisters and four brothers. Their support was really crucial to me to accomplish my studies abroad.

Contents

List of Figures

Abbreviations

FSR	Free Spectral Range
TIR	Total Internal Reflecation
LASER	Light Amplification Simulation Emision RRadition
CMOS	Complementary Oxide Semicondutor
CMOS	Complementary Oxide Semicondutor
LED	Light Emiting Diode
LED	Light Emiting Diode
WDM	Wavelength Division Multiplexing
LED	Light Emiting Diode
RI	Refraction Index
LED	Light Emiting Diode
TEW	Transverse Electrical Wave
TMW	Transverse Magnetical Wave
WGM	Wispering Gallery Mode
FWHM	Full Width Half Maximum
ELISA	Enzyme Linked Immunoe Ssays
PCR	Polimer Chain Reaction

Physical Constants

$$\text{Speed of Light} \quad c \quad = \quad 2.997\ 924\ 58 \times 10^8 \text{ ms}^{-\text{S}} \text{ (exact)}$$

Symbols

Symbol	Name	Unit
a	distance	m
P	power	W (Js^{-1})
ω	Angular frequency	rads^{-1}
V	Volume	Liter
h	Height	Meter
λ	Wavelength	Meter

Chapter 1

Introduction

1.1 Motivation

Considerable demand for far-reaching of sensing systems have been significantly advancing recently. These improvements make the monitoring and detecting nanoscale objects easier and without any chemical labels. This advancement is achieved mainly for applications in health sector, land security, drug discovery, air pollution, and diagnostics. Due to their small size and low refractive index contrast with the surrounding medium, most nanometer size objects possess a low polarizability. It can provide only weak and undetectable light to matter reactions, making these label-free sensing of nanoparticles much more challenging. However, combining a high quality factor (Q) and a small mode volume (V) lead to micro and nano-photonic devices having highly sensitive platforms. This implementation results in the considerable enhancement of interaction between light and matter. Optical resonators have been used to identify individual nanoparticles that have a radius of lower than 30 nm by monitoring the transmission spectrum. Increasing Q-factor of resonator can be reached a narrower linewidth, which leads to smaller changes in the transmission spectrum as well as it significantly improves their performance [1].

Nowadays, new evolutions in the Micro and Nano technologies give rise to potential applications with unprecedented control in a wide range of varieties. Optical micro-resonators with a high Q factor are excellent candidates for optical manipulation and they can be

fabricated in low cost. They can also have significant enhancement of detection in bio-sensing and other applications that use lasing light sources. Therefore, these advancements in design and materials such as nanowires and 3-D photonic crystals are bringing to further levels of advancements. Apparently, it will impact the future growth of broadband for all-optical networks, also for basic researches in quantum physics. However, the progress of resonator-based platforms in the near future can impose strict criteria on their design, fabrication and manufacturing process [2].

Ever since their inventions, Optical Micro-resonators set a high promise as fundamental building blocks for a variety of applications in optics, photonics, telecommunications and other fields. Ring resonators are proven to be very successful in sensing field. In this manner, they are enhancing their focus on the contemporary researches [3]. One of the main advantages of utilizing ring resonators as bio-sensing platforms is the opportunity of fabrication in minute size. They can be used to target any sample that need to have results in easier ways by using Raman spectroscopy and related ones.

During modeling and design process, many aspects should be taken into consideration and should make compromises between various parameters. Common parameter combinations considered are the Q factor and the size of the resonator, distance between the waveguides, alignment in a point where the light coupling gets easily initialized. Furthermore, input lasing wavelength, core and cladding material properties (such as Refraction Index), deformation of notch cavity, and many other properties that are other crucial factors towards a better functional system.

In this respect, our motivation is based on the idea to develop a simulation-based high sensitive model towards nanoparticle bio-detection. This is realized by using the phenomena of lasing light that were applied in optical ring microresonators. Sensitivity mechanism is based on the shifts which are caused by binding individual ânano-beadsâ. They are positioned in any liquid solution in a size characterization at lowest radius of approximately 10 nm, which is the size that is approached to be a single molecule. The graph of that resonance shift versus the transmitted light reveals information of binding event. The binding particles can be characterized by the value of shifted resonance.

In general, an attempt to develop a highly sensitive biosensor by using optical micro-resonator based on laser light is made. The reason for micro-resonator selection is attributed to their label-free methods, operation in real-time and their ability to be

characterized as small molecules by assuming them as engineering material. Important detection restrictions are mostly set by laser linewidth, which can be adjusted to be more narrowed than the resonance width. In the other words, these types of sensors that utilize lasing light have the possibility to detect targeted objects that are in ultra-small size.

1.2 Basic sensing operation

In the recent decades, we have seen an emerging transition from electronics field to photonics in both academic research and industry. Starting from electronics which was the area that played a dominating role in semiconductors at the middle of the last century, also photonics pretends to be a great factor of bringing the humankind in the new era of information and technology [4]. The aim of photonics, as a discipline of science, is to control and manipulate the optical properties of materials in analogy to electrical properties of semiconductor one. Therefore, photonics is a field of physics which deals with the control of the light or photons, for useful applications including light generation, detection and manipulation emission as well as with transmission, modulation, light signal processing, amplification or sensing [5]. Photonics is a broad area which investigates and develops ideas about light interaction since from the first practical semiconductor photons (light) emitters, invented in early of the 1960s and optical fiber developed in 1970s [6]. Latest advances in artificial materials structure over and beyond the deep qualitative understandings of the light itself as dual physical nature either as classical or quantum physics, were a great opportunity to provide the possibility of well manipulating and processing a light-signal.

Light is an electromagnetic radiation within a range of frequencies starting from 1 THz to 10 pHz. Visible light, which is perceptible by the human eye consists of a scaled wavelength range of 400-700 nanometers (nm), and is defined as the color range between violet through red region. In this matter, it is in photonic devices interest to be able to practically work in this range of frequencies since most of them are engineered to be compatible in invisible and near of infrared wavelengths. Another important factor that gives a contribution to properly functionalities to an optical wave is photon energy. For visible light, the energy of photon lies between values of 1.7 and 3.1 eV. Moreover, photonic devices which are mainly focused in process of generating, amplifying or detection

of the light are more important to know about the nature of the light, whereas the physical nature of the wave is essential at post-processing light-signal such as transmission, modulation, or switching [5].

One of the very considerably explored devices in recent years that combine optical and photonic properties for their principle operation is optical microresonators. Optical microresonators as essential building blocks of devices for a wide range of implementations in the discipline of photonics have shown a high potential use in many applications such as lasers, amplifiers, sensors, optical add/drop (de)multiplexers (OADMs), switches, routers, logic gates, and artificial media. The simplest configuration framework consists of a couple of standard waveguides (optical fibers), of which, one is of a straight form and the other is circular, and are produced in micron-scale geometry such as microsphere, microtoriod or microring (or disk, ellipse, rectangle, and circle). As the main focus of this work lies in the microring geometry, here we will explore this model in more details. In this manner, setting the waveguides to be aligned in the vicinity of each other, or in some implementations as integrated ones at a point, the light will be guided through the circular fiber, in order to channel the light that will be travelling in the closed loop formation, leads by the shape of the resonator. Also, the loop line of the light footage takes the waveguideâs form (see Figure 1.1). If the waveguide is in the form of a ring, the microresonator is mere a circular closed loop, forming a cavity, which can sustain both transverse and longitudinal propagation mode [7].
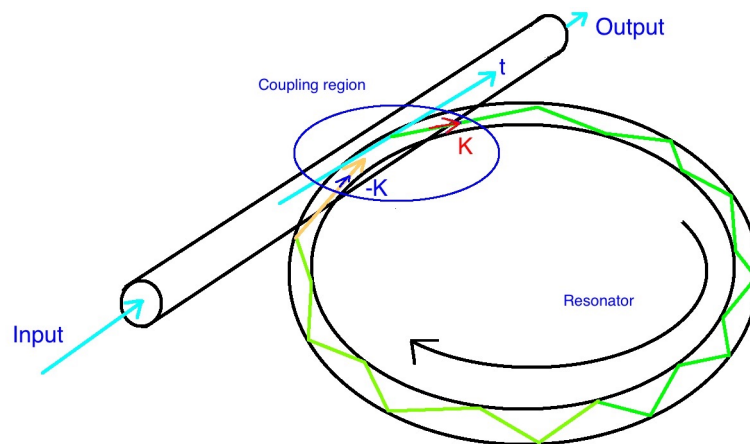
FIGURE 1.1: A schematic representation of ring resonator and coupling coefficients

It is well known that light can be confined even in any transparent material (e.g. classic glass) by reaching some opto-physical conditions, such as the angle at which causes the outer edge to be lower than a specific deterministic angle, defined by the refraction index of the inner transmitting medium and the surrounding media. While the light is reflected, it remains inside the waveguide owing the phenomenon known as total internal reflection (TIR). TIR occurs when the light strikes the boundary media and fails to refract through it. In the classical picture, optical resonators deal with some specific waves known as Eigen-modes of a wave field inside of a given smooth edges cavity. They consist of waves circulating around the cavity, propagating through the circular waveguide and after one round-trip they return to the same point and the same phase (modulus 2π). Henceforward, these waves interfere constructively with themselves, creating standing waves and consequently meet the resonance condition. These resonances depend highly on the resonator cavity geometry [8, 9].

Next, it induces another evanescent wave in the outer medium that propagates tangentially to the surface and extends around 200 nm outward [10]. When the resonance effects of the light within the microresonator, this light builds up an intensity inside the ring-shaped media through multiple round-trips and is available through another phenomenon, known as Light Coupling.
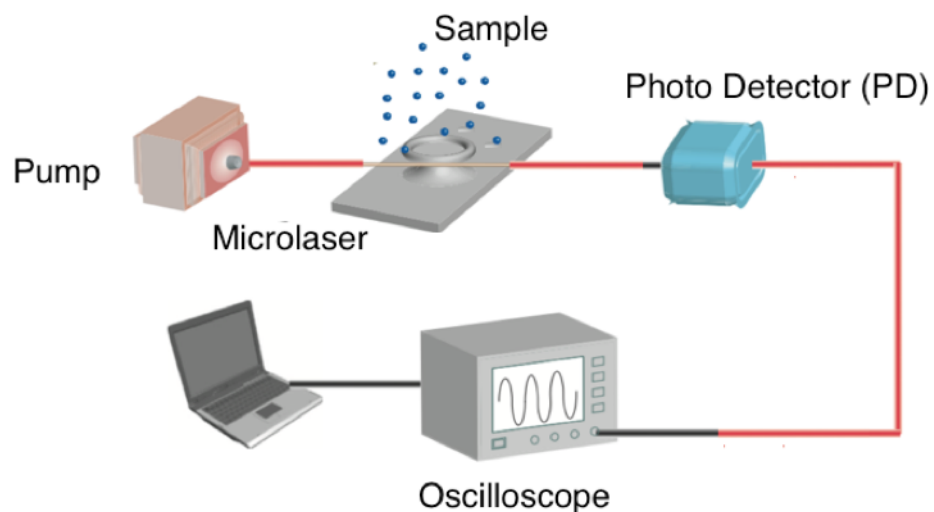
FIGURE 1.2: A setup for application of micro-resonator-based for nanoparticle analysis.

The resonance state is very complex itself and crucial for the operation of the optical resonators as well. In the closed loop, only some of selected wavelengths will contribute

onto the resonance of that light. A portion of light that did not match the resonance condition will continue its pave directly to the output bus waveguide where it performs the light output. In this point is perform the transmitted light and measurement of the spectra. Due to this phenomenon, the optical resonator can play the role of a filter as well as optical sensor [11] . In this work, optical sensors are going to be analyzed more profoundly.

Optical ring resonators operation rely on many physical principles, where three of them are essential: Total Internal Reflection (TIR), Constructive Interference and Optical Coupling. Each of these are independent topics related to ring resonator and will be discussed in the following chapters of this thesis

1.3   Literature Review

In the late of 19th century Maxwell has proposed a theory called Radiation Pressure Theory that is related to electromagnetic interaction for any given surface. The existence of this extremely small optical force was described by a physicist, Peter Lebedev, in 1901. In the next half of century, this field has been relatively slow due to the issues about the ways to impact in particles. Therefore, this field started to revive itself again especially after the invention of the light amplification for stimulation of emission of radiation, known as LASER, during the 1960s. After this invention, it took to a high light intensity and boosting radiation pressure which opened the doors to numerous developments in this field [12]. Optical microresonator as a waveguide-based device was firstly demonstrated by the work of scientists Weber and Ulrich, in 1971. This device was constructed by a 5-mm diameter glass and covered with Rhodamine-6G-doped polyurethane. The light coupling was arranged by a prism and light was provided by a laser at wavelength ($\lambda = 337.1nm$), which come up with a laser operation. This demonstration was then followed by another one by Haavisto and Pajer in 1980. The new device consists of integrated bus waveguides made with a doped polymethyl methacrylate film in the substrate of quartz. What was novel at that time is the fact that in their work they did not use the process of lithography for their fabrication process, but only direct-writing with a He-cd laser. Despite this method, most of the issues lied in deviceâs size, which was in a total circumference of 28.3 cm. Beyond all these pros and cons, the essential idea had finally been established [7].

A new demonstration at that time was firstly done by Stokes, Chodorow and Show, in the beginning of 1980s. This was the optical glass fiber resonator [13]. These types of resonators were not able to be integrated to the other optical blocks because of their long circumference that was near to 3m. After this glass-based demonstration, the decade was dominated by similar implementations, either by individuals or a group of scientists. The main challenge for that time was optimization of the size and the issues about glass material. By the end of this period some efforts led us to the reporting of multiring filters, constant temperature operation and similar studies.

In the early of 90s, the science community gave huge efforts to bring about a new era for microresonators, which started to take into consideration a new way of fabrication by chemical elements of group III-IV of semiconductors. Developments in the semiconductor industry, which has been used mostly in electronics in CMOS technology and the similar ones, were a strategic initiative to provide a powerful basement for a new way of fabrication in the field of photonics and related ones. With this technology, scientists were able to think for tiny size produced elements, even in diameters that were comparable to or less than the wavelengths (down to micro and nanometer) itself. In 1993 for the first time it was reported about a demonstration of microdisk laser with three InGaAs/InAlGaAs quantum wells. These lasers with 20 μm in diameter with a single mode at 1.5 μm wavelength were optically pumped with pulsed Argon-ion and have been fabricated by the selective etching method [14]. These early efforts did not have the ability to include bus waveguides in their operation. Therefore, they were based on fibers that collected the light directly from the disk. Similarly, the first microring- geometry resonator with a diameter 20.5 μm, reported to be constructed from a novel semiconductor waveguide-coupled to bus waveguides, which used a material such GaAs-AlGaAs. This was implemented in 1997 by Rafizadeh at Northwestern University [15]. After this, many of groups were able to bring off demonstrations about literally and vertically coupled ring by GaAs-AlGaAs started to be used as important integrated photonic blocks such as switches, routers, and both multiplexers/DE-multiplexers logic operation.

With regards to ring resonators, in the last decades there are many PhD dissertations devoted to the study, modeling and fabrication in different systems of materials. Some of them comprised of integrated rings, spheres and disks resonators is bringing by Rafizadeh (1997), with the material of AlGaAs/GaAs are developed and fabricated. In years of around 2000, another resonator project based on the system AlGaAs/GaAs materials is

conducted by Absil, with multiple coupled ring resonator configurations are manufac-
tured, with vertical and lateral coupling. For the resonator gain had been carrying on
dissertations of Djordjev (2002) and Rabus (2002), built by InP material system. Other
optical amplifiers (SOA) are presented in integrated semiconductor technology, that later
made possible of modifications as filter functions. With material of InP, those resonators
were with smallest circumference of only 20 μm, are bringing by the dissertation of Grover
(2003). A research about nonlinear properties of InP-based ring resonators is presented
in the thesis of Ibrahim (2003). After several years the author published a book with
the same thematic. A common thing for all those devices was that all of them had
been conducted in materials of semiconductors or dielectrics. In thesis of Rabiei (2003),
are fabricated ring resonators in electro optic polymers used as modulators. Polymer
resonator modulators are also demonstrated in Leinse (2005). These works are exam-
ples of currently ongoing researches about ring resonators, expanding their potential for
application and are going to deal with in following chapters of this thesis dissertation [3].

In recent years, these types of devices have become more important as potential appli-
cations due to their compatibility for integration in micro and nano sized systems.

In summary of historical context and literature review, the first proposal for microring
resonator was made at the 1960s, and circumference varied at high values, started
from microns to meters. They were widely applied in communication systems as inte-
grated blocks of photonics circuits. These types of resonators became rapidly a potential
candidate for photonic devices as dropping filters, WDM de-multiplexers, and ON-OFF
switches, light-emitting diodes (LEDs). Lastly, optical ring resonators started to see high
attention by scientific community that found them attractive for scientific and engineer-
ing purposes, mostly for biochemical sensing and either in Micro/Nano particle detection
or monitoring as well [16].

1.4 Thesis Objectives

Optical ring resonators are worthwhile applicable devices that can find a wide range of
usage, in many areas of technical variety. Therefore, the main objective of this thesis
is to study and develop a simulation-based model for ring resonator as biosensor device

for biomolecules/nanoparticle detection. A 2-Dimensional visualized model is then introduced to study and simulate the ring resonator operation, to bring results in a better perspective. Additionally, here are presented some unique results for the ring radius value and linear sensing response for certain mimic bio-agents.

This work is divided in several parts:

i) General waveguides principles, with main focus in optical resonators,

ii) Manipulations of optical ring microresonators,

iii) The corresponding results, discussions and conclusions are based on the simulation which is run by COMSOL Multiphysics Tools v.5.2.

The goal of this thesis work is to present a built model platform for nanoparticle sensing as well as to optimize the performance of microresonator. The specific steps in this research include:

1. Modeling and simulating an optical ring microresonator: The resonator radius is modified to include an extra thin layer of the same material around the ring, both inside and outside. This is implemented in order to mimic the binding of biomolecules/nanoparticles around the resonator. The simulations for this part are performed in the range of to in size. It is important to note that the material of the attached nanoparticles/biomolecules is having the same properties as the material of the ring. Hence, a linear correlation between the variation of the ring radius and the transfer function shift is observed.

2. Optimizing the resonator operation performance: This step includes improving the resonator operation performance at the expense of other parameters. It involves using multiple simulation measurements, graphs, and figures for optimization process.

3. Similar to the first part, a thin layer around the ring is extended but also varying the concentration of biomolecules. Variation in the biomolecule concentration changes the refractive index of the modified layer. Hence, there are 2 parameters to be considered namely the size of the layer and its refractive index. Different combinations of the size and refractive index variations are simulated and the spectrum of the resonator response is monitored. The Yamaguchi effect model is also taken into account for the effects of refractive index. Simulations are performed using two kindsâ materials: Titanium Dioxide Nanoparticle ($RI_{TD} = 2.41$) and Protein Biomolecule ($RI_{PB} = 1.45$) [17].

All the three objectives will be detailed out in the results and discussions chapter.

Chapter 2

Theoretical Fundamentals of Optical Dielectric Waveguides and Optical Microresonators

2.1 Reflection and Refraction of Plane Wave

2.1.1 Snell's Law

For a plane wave, there are some well-known phenomena about reflection and refraction, when light strike a plane interface between two quality different mediums. In those cases, the light wave will be separated in two waves, the one which is transmitted straight to the second media and the one which does not pass the boundary, remains within the first media, or in other words is reflected. Additionally, Snellâs law provides a mathematical apparatus in order to describe the behavior of a wave light when it faces any interface of two the different mediums. Let assume that and are refraction indices of medium 1 and 2, the magnitude of the wave numbers consists of

$$|\vec{k_i}| = |\vec{k_r}| = \frac{\omega}{c} \times n_1, \tag{2.1}$$

$$|\vec{k_i}| = \frac{\omega}{c} \times n_2. \tag{2.2}$$

Basically, these equations yield on the kinematic properties of the both, reflection and refraction effects. Then, with and represent the corresponding incidence, reflected and transmitted, is depicted by the letters, respectively. For the wave with respect to the normal plane of a given interface, is described by the following expressions

$$n_1 sin\theta_i = n_1 sin\theta_r = n_2 sin\theta_t. \tag{2.3}$$

In this equation we can see that the angle of reflection must be equally to the angle of incidence, from which we obtain the Snellâs law:

$$\frac{sin\theta_i}{sin\theta_r} = \frac{n_2}{n_1}. \tag{2.4}$$
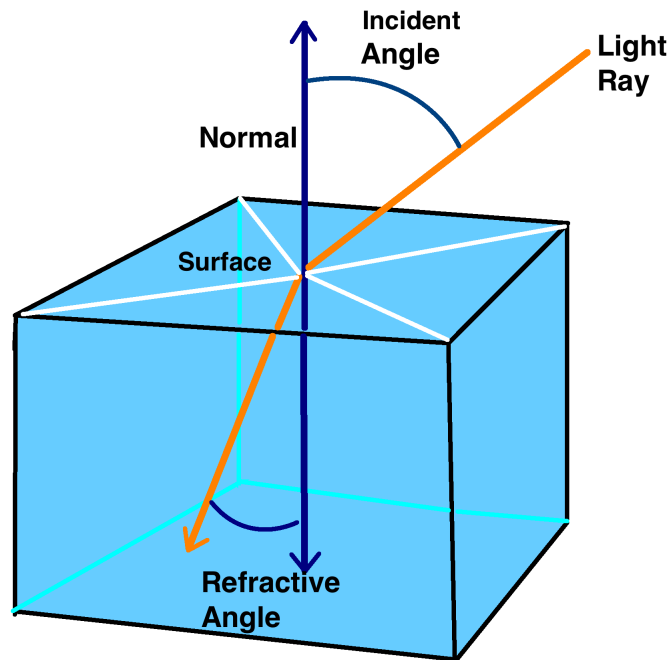
FIGURE 2.1: A schematic representation of Snell's Law. Two different media. Reflected and refracted waves are depicted

2.2 Reflection and transmission of s wave (Transverse Electrical wave) (TE)

Transverse Electrical wave wave is known also as 's' wave. This is based on the fact that electric field vector $\vec{E}$ is transverse to the incidence plane [18]. This 's' letter most probably comes from the German word 'Senchreht' which means something that is perpendicular to something else. In this case, all the electric field vectors are perpendicular with respect to the plane of incidence, and magnetic field vectors are chosen to give a positive contribution towards the direction of wave vectors.
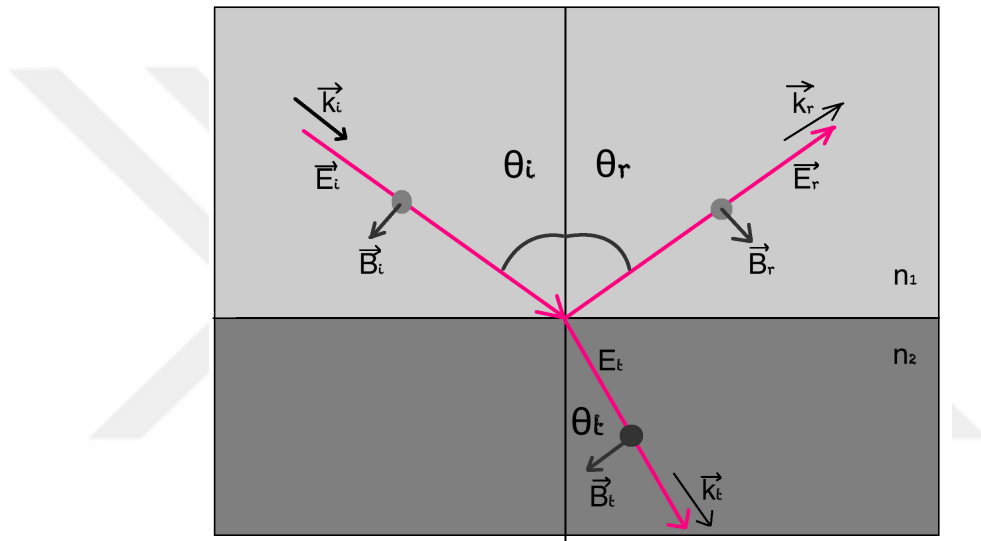
FIGURE 2.2: A 's' wave incoming for the medium 1, a portion of that remain in the same media and a portion is refracted and transmitted to the second media

To reach the interface effect, it should fulfill the boundary conditions, and expression comprises to

$$\frac{n_i}{\mu} \times (\vec{E_0}i - \vec{E_0}r) \times cos\theta_i = \frac{\eta_t}{\mu_t} \times \vec{E_0}t \times cos\theta_t \qquad (2.5)$$

From the equation of field vectors:

$$\vec{E_0}i + \vec{E_0}r = \vec{E_o}t, \qquad (2.6)$$

we have:

$$\left(\frac{\vec{E_o}r}{\vec{E_o}i}\right)_\perp = \frac{\frac{\eta_i}{\mu_i} \times \cos\theta_i - \frac{\eta_t}{\mu_t} \times \cos\theta_t}{\frac{\eta_t}{\mu_t} \times \cos\eta_i + \frac{\eta_t}{\mu_t} \times \cos\eta_t} \tag{2.7}$$

and

$$\left(\frac{\vec{E_o}t}{\vec{E_o}i}\right)_\perp = \frac{2 \times \frac{\eta_t}{\mu_i} \times \cos\theta_i}{\frac{\eta_i}{\mu_i} \times \cos\theta_i + \frac{\eta_t}{\mu_t} \times \cos\theta_t} \tag{2.8}$$

After regulation, we have

$$r_\perp = \left(\frac{\vec{E_0}r}{\vec{E_0}i}\right)_\perp = \frac{\eta_i \times \cos\theta_i - \eta_t \times \cos\theta_t}{\eta_i \times \cos\theta_i + \eta_t \times \cos\eta_t}, \tag{2.9}$$

and

$$r_\perp = \left(\frac{\vec{E_0}r}{\vec{E_0}i}\right)_\perp = \frac{2 \times \eta_i \times \cos\theta_i}{\eta_i \times \cos\theta_i + \eta_t \times \cos\theta_t}, \tag{2.10}$$

By deducing the equations, we have obtained the last expressions for applying to any media which can be linear, isotropic and homogenous. This is done under the assumption:

2.3 Reflection and Transmission of p Wave (Transverse Magnetic Wave) (TE)

This type of polarization is called P polarization. It is also known as TM wave because magnetic field vector is perpendicular to a given incidence plane. Herein, all the electric field vectors are in the incidence plane, and the other part of magnetic field vectors are in positive plan of energy flow toward propagationâs direction.

In a similar way of deriving equations as in the previous case of wave polarization, also p type should impose the continuity of electric and magnetic field. The expression that denote this contains the following members

$$\frac{\vec{E_0}i}{\mu_i\nu_i} + \frac{\vec{E_0}r}{\mu_r\nu_r} = \frac{\vec{E_0}t}{\mu_t\nu_t} \tag{2.11}$$

By taking the assumption:$\mu_i = \mu_r$ and $\theta_i = \theta_i$, in order to obtain:

$$r_{\parallel} = (\frac{\vec{E_0}r}{\vec{E_0}i})_{\parallel} = \frac{\frac{\eta_i}{\mu_i} \times \cos\theta_i - \frac{\eta_t}{\mu_t} \times \cos\theta_t}{\frac{\eta_i}{\mu_i} \times \cos\theta_i + \frac{\eta_t}{\mu_t} \times \cos\eta_t}, \tag{2.12}$$

and

$$t_{\parallel} = (\frac{\vec{E_o}t}{\vec{E_o}i})_{\parallel} = \frac{2 \times \frac{\eta_t}{\mu_i} \times \cos\theta_i}{\frac{\eta_i}{\mu_i} \times \cos\theta_i + \frac{\eta_t}{\mu_t} \times \cos\theta_t}. \tag{2.13}$$

In the case of non-magnetic media, for the both parts we have:

$$r_{\parallel} = (\frac{\vec{E_0}r}{\vec{E_0}i})_{\perp} = \frac{\eta_t \times \cos\theta_i - \eta_i \times \cos\theta_t}{\eta_i \times \cos\theta_t + \eta_t \times \cos\eta_i}, \tag{2.14}$$

and

$$r_{\parallel} = (\frac{\vec{E_0}r}{\vec{E_0}i})_{\perp} = \frac{2 \times \eta_i \times \cos\theta_i}{\eta_i \times \cos\theta_i + \eta_t \times \cos\theta_t}, \tag{2.15}$$

The last two expressions represent a general application for any two given different media. In the other words these are also known as Fresnel equations, r_s, r_p, are the Fresnel reflection coefficients, t_s and t_r, are the Fresnel coefficients of transmissions [11].
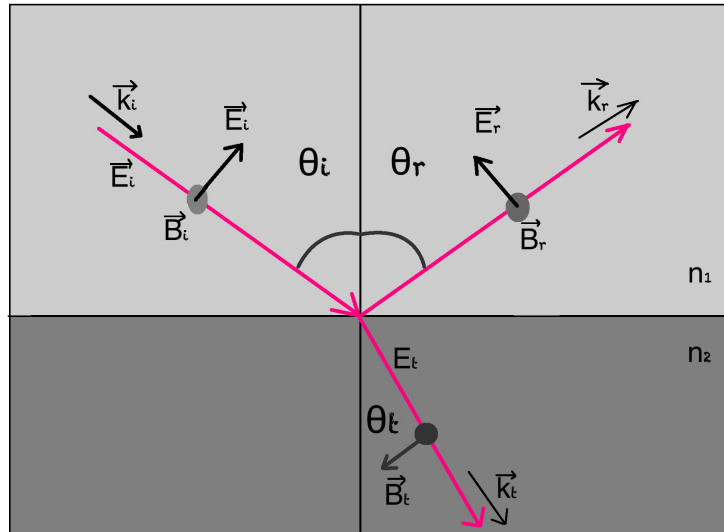
FIGURE 2.3: A 'p' wave incoming for the medium 1, a portion of that remain in the same media and a portion is refracted and transmitted to the second media

2.4 Reflectance and Transmittance

Despite of the fact that Fresnel formula provides the possibility to characterize the amplitude of the incident wave, in some cases we need to know how much energy is reflected from the boundary and is transmitted to the next medium. For this reason, we should take on consideration the ratios of Poynting vectors of power flow, for the reflected and transmitted waves to that incident wave [19]. The power which circulates in a parallel way to the boundary surface tends to be unchangeable throughout the medium. Hence, as our main concern is to deal with reflection and transmission, we can consider only the normal components of Pointing vectors. In this sense, reflectance and transmittance consist of

$$R_s = |\frac{\chi S'_{1S}}{\chi S_{1S}}|, \ R_p = |\frac{\chi S'_{1p}}{\chi S_{1p}}|, \tag{2.16}$$

and

$$T_s = |\frac{\chi S'_{2S}}{\chi S_{1S}}|, \ T_a = |\frac{\chi S'_{2p}}{\chi S_{1s}}| \tag{2.17}$$

From the last expressions, S represent the time-averaged vector of Poyting, and media is denoted by number 1 and 2, as well as S and P denote s and p waves, respectively. X is the unit vector

$$S = \frac{\vec{k}}{2\omega\mu} \times |\vec{E}|^2, \tag{2.18}$$

By assuming the medium is dielectric, the refraction index - η is a real number, is the wave vector, and is the amplitude of the plane wave. Reflectance and transmittance are related to the Fresnel coefficients [19] by

$$R_s = |r_s|^2, \ R_p = |r_p|^2 \tag{2.19}$$

Consequently, we have:

$$T_s = \frac{n_2 \times \cos\theta_2 |t_s|^2}{n_1 cos\theta_1}, \tag{2.20}$$

and

$$T_p = \frac{n_2 \times \cos\theta_2 |t_s|^2}{n_1 cos\theta_1} \tag{2.21}$$
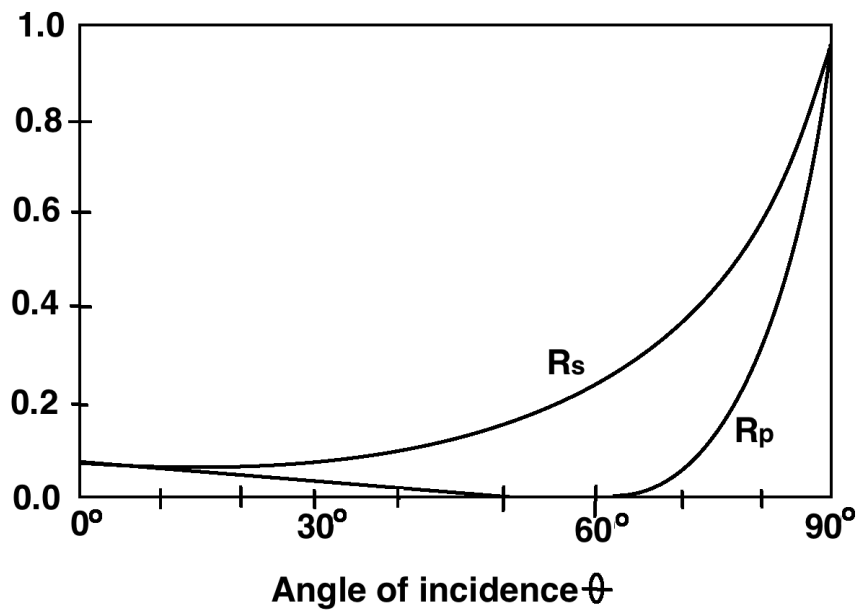
FIGURE 2.4: Reflectance R_s and R_p as function of θ for $n_1 = 1.0$ and $n_2 = 1.5$.

2.5 Optical Waveguides

Optical waveguides represent some of the basic elements for light confinement and transmission throughout a variety of distance, starting from tens of micrometers, that can find implementation in many integrated photonic devices, to hundreds or thousand miles in long distances fiber-optic transmissions. They are important sections for connection

of many photonic devices, some of them are fundamental such as light couplers and modulators.

The structure of an optical waveguide consists of a longitudinally lied in a high index medium, which is called *Core*. This medium is longitudinally surrounded by another media with different characteristics, such as lower-index media and is called *Cladding* [5]. An optical waveguide they can take the form of a slab, strip or cylinder that is fabricated by dielectric material.
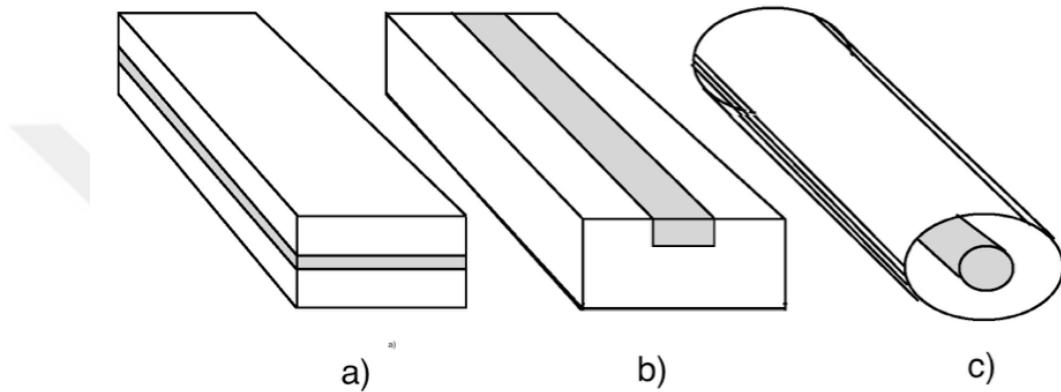
FIGURE 2.5: Optical waveguide form where the grey space represents the high indexed medium or core, which is surrounded by lower index media-cladding; Forms: a) Slab, b) Strip and c) Cylinder

Lets consider the straight waveguide, of which the longitudinal part is given in z- direction. Specifications of this waveguide are inferred by transverse directions of its dielectric constant , which has two freedom states in x and y direction, and are independent to the z-coordinate. Based on this fact, we can take a characterization for both dependent variables to a single spatially dependent transverse profile of refraction index, .

For the case of non-planar waveguide, the core is surrounded by cladding in all transverse directions, such the characterization profile in function , which is dependent of x and y coordinates. When it is the planar, it has a optical confinement only in one direction, the surrounded medium is chosen to be as a sandwich-like around the core and between the layers. The core of a slab or planar waveguide is called film. The upper part of the core that in a form burry the core part, is called cover, and the bottom part that represent the basement of all waveguide, is called substrate. All that terminology come into the form during the fabrication process.

As for index profile, a waveguide in which this element has a rapid change between the interfaces of core and cladding, is called Step-index waveguide. In the other case which this profile has more linear change, is called Graded-index waveguide. This differentiation is done due to the flaw change process in the gradual trends and both of them are illustrated in the following figure.
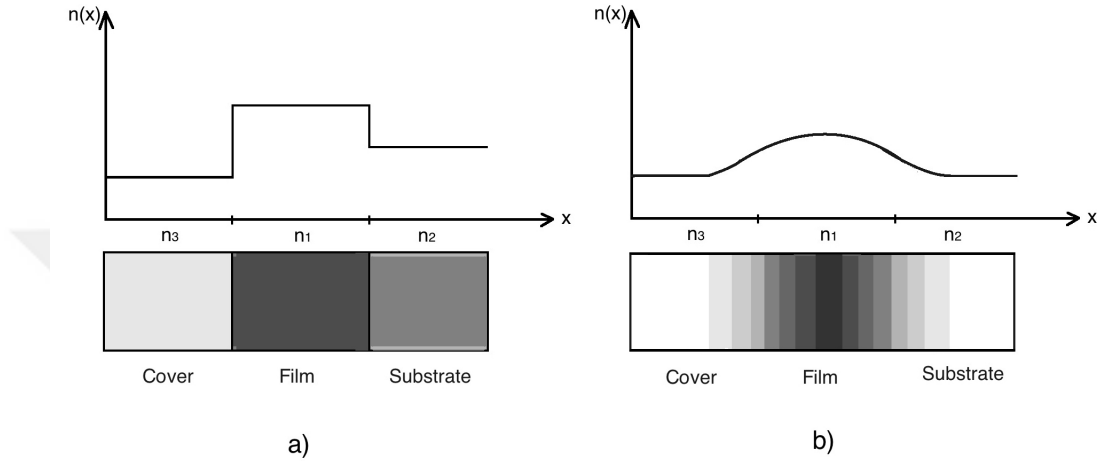
FIGURE 2.6: A graphically illustration of two types of waveguide in terms of Index Profile variation: a) Step-Index waveguide and b) Graded-Index waveguide

Another characteristic is waveguide mode. Modes exist for a particular structure and is the transverse field pattern that has an amplitude and polarization profile that is constant during the longitudinal of z coordinate. The expressions for electric and magnetic fields are given by

$$\vec{E}_\nu(r,t) = \vec{E}_\nu(x,y)e^{i\beta_\nu z - i\omega t}, \tag{2.22}$$

$$\vec{H}_\nu(r,t) = \vec{H}_\nu(x,y)e^{i\beta_\nu z - i\omega t}, \tag{2.23}$$

where, ν - represent the mode and are the mode field profiles and in this case β is propagation constant of the mode. For the case where waveguide has its transverse confinement in both dimensions: x and y, with two scale of degree of freedom, the mode index ν is symbolize of both parameters of field variations of the mode fields. For the

case of planar mode, fields do not vary with the y coordinate

$$\vec{E}_\nu(r,t) = \vec{\varepsilon}_\nu(x)e^{i\beta_\nu z - i\omega t},$$ (2.24)

$$\vec{H}_\nu(r,t) = \vec{H}_\nu(x)e^{i\beta_\nu z - i\omega t}.$$ (2.25)

From these expressions, mode fields depend only in x coordinate. Hence, ν characterize x-coordinate.

Wave guidance in inside of dielectric waveguides is mostly result of the optical phenomenon called Total Internal Reflection (TIR)[7]. When the light is reflected within the core space, it faces some striking to the core-cladding interface in an angle greater than critical angle. For most of the waveguide cases, this condition is satisfied when a light which comes to the input of core, at an angle smaller than waveguideâs acceptance angle (in terms of guideâs propagation axis). The critical angle is determined by the Fresnel equations, which are combined then with Maxwell equations in order to apply boundary conditions for the electric and magnetic fields. For reflectivity, is used the Fresnel expression for any angle of incidence inside the critical angle for TIR, as following

$$r_{TE} = \frac{n_1 \cos\theta_1 - i\sqrt{n_1^2 \sin^2\theta_1 - n_2^2}}{n_1 \cos\theta_1 + i\sqrt{n_1^2 \sin^2\theta_1 + n_2^2}} \equiv e^{-i\Phi_{TE}}$$ (2.26)

and

$$r_{ME} = \frac{i\frac{n_1}{n_2}\sqrt{n_1^2 \sin^2\theta_1 - n_2^2} \cos\theta_1}{i\frac{n_1}{n_2}\sqrt{n_1^2 \sin^2\theta_1 + n_2^2} \cos\theta_1} \equiv e^{-i\Phi_{TM}}.$$ (2.27)

Where, transverse electrical (TE) represent the light linearly polarization which the electrical field consist of perpendicular to the incidence plane as well as transverse magnetically represent the perpendicular plane of wave incidence (TM), respectively.

Regarding to reflection and refraction there are three important modes for dielectric waveguide. For simplification, we consider the wave as a ray in terms of qualitative behavior for an asymmetric planar waveguide. For refraction index of the waveguide layers, we have three constants: n_1 ,n_2 and n_3. Based on the Figure 2.2, $n_1 > n_2 > n_3$. If we define the angular frequency ω, and wavelength λ, the mediums of the waveguide is defined by constant:

$k_1 = n_1 \times \frac{\omega}{c}$, $k_2 = n_2 \times \frac{\omega}{c}$, and $k_3 = n_3 \times \frac{\omega}{c}$, where , $k_1 > k_2 > k_3$.

Since in inside of the waveguide are three different media, there are two critical angles related to total internal reflection at upper and beneath part (cover and substrate). Total internal reflection angles for down and upper interfaces are given by expressions, respectively:

$$\theta_{c2} = \sin^{-1} \frac{n_2}{n_1} \tag{2.28}$$

and

$$\theta_{c3} = \sin^{-1} \frac{n_3}{n_1}. \tag{2.29}$$

Since, $n_2 > n_3$ also, $\theta_2 > \theta_3$. This depends on reflected angle of the incidence angle θ, and we can get the characteristics of reflection and refraction. Based on that we get the three characteristic modes: Guided Mode, Substrate Radiation Mode and Substrate-Cover Mode.

1. Guided Modes, for: $\theta > \theta_{c2} > \theta_{c3}$. In this case light is totally reflected inside the core in both the upper and bottom interfaces, consisting in a guided mode. By a huge number of reflection by the ray wave, at some points it can interfere constructively by itself. This can occur only when a transverse resonance condition is reached, so that is repeatedly reflected wave. The x component of the wavevector is: $k_1 \cos \theta$, with an angle of incidence θ and the z component consist of $\beta = k_1 \sin \theta$. For a round-trip transverse arcade with a core thickness d, the phase shift is:$2k_1 d \sin \theta$. Also, here exist phase shifts φ_2 and φ_3 for every single term of wave reflection in the upper and bottom place of the

waveguide. Since, φ_2 and φ_3 are functions of θ , it can be reach resonance phenomenon for constructive interference. In a round-trip transmission part, we have

$$2k_1 d \cos\theta + \varphi_2(\theta) + \varphi_3(\theta) = 2m\pi \tag{2.30}$$

where, m is an integer number. There is a characteristic case where m=0, where this case consist in fundamental mode. For m greater than zero, are high-order modes. Figure 2.3 a) and 2.3b).
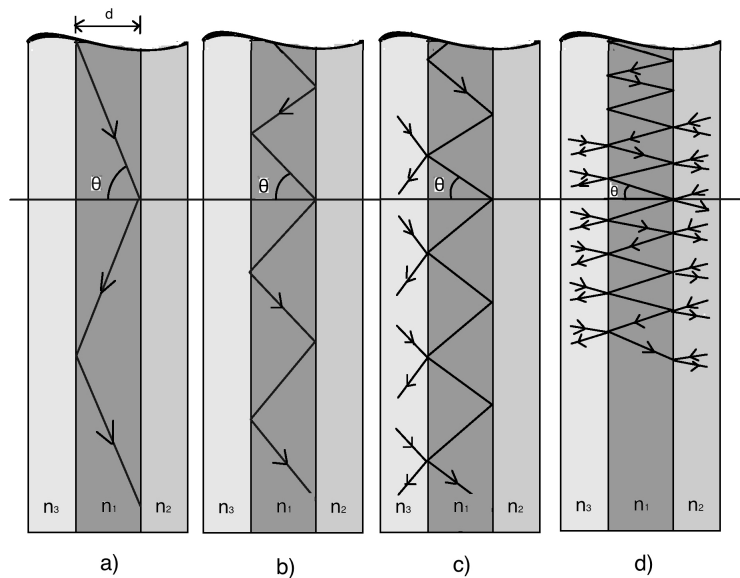
FIGURE 2.7: A represantation of Total Internal Reflection in different critic angels

2. Substrate radiation mode, for: $\theta_{c2} > \theta > \theta_{c3}$. As shown in Figure 2.3 c), total internal reflection can be reached only for the other part of waveguide (in right side of the graphic). Therefore, in the other part light is refracted. This wave is not confined inside the core and after a portion of waveguide it will be disappear.

3. Substrate-cover radiation modes, for $\theta_{c2} > \theta_{c3} > \theta$. In this case, we do not have total internal reflection, at all. Light wave comes from entrance of waveguide faces some incidence across the core, where refraction phenomenon is present in both sides. The modes are not discrete and leave values of forming a continuum between k_3 and 0, Figure 2.3 d).

With respect to the first case of reflection (the guided mode), TIR is really 'total' in the sense that no energy is lost along the process of reflection. Although, when this property is performed in any real device or waveguide, there always will be a part of the light losses due to absorption and reflections that occurs at the surfaces where the light strikes and passes the medium. However, TIR presents a fundamental mechanism for confining the light inside of an optical waveguide [7].

2.6   Theory of Optical Coupling

When two waveguiding structures are aligned in the vicinity of each other, an optical power exchange between their supported modes is established. The analysis for this phenomenon can be proceed by treating the normal modes of the waveguides as equivalent and considering them as to be individuals. When there is only a waveguide of a single-mode, both symmetric and antisymmetric ones contain solutions for a given coupled structure. In general, there is a difference between the two modes and it consists of different propagation constants. When the total power as initial condition is positioned only in a waveguide we can approximate as one particular superposition of the symmetric and antisymmetric wave mode, by adding them synchronously. Based on the fact that both modes are in different wave velocities, in some wavelength (âBeatâ length) the exchange between the guides exists and a transfer of the optical power to the other waveguide comes in function. This effect takes part forth, while the two guides cores maintain their closing position to each other. This phenomenon is illustrated in following Figure 2.8 [7].

The beat lengths are some parameters that are in function of the separatiton distance to the cores. These modes will definitely not couple in the case when the cores are far apart to each other, and the beat length is infinitely long. Coefficients of coupling can be computed via the effective indices of the symmetric and asymmetric modes or alternatively by utilizing the modes of the individual guides and then applying a perturbation-method approach, as describes more in details in [19].
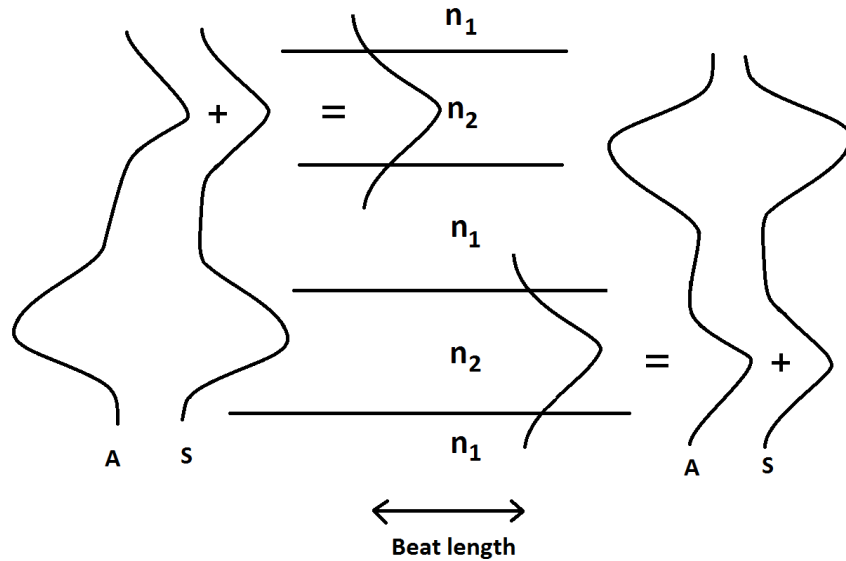
FIGURE 2.8: A representation of coupling effect for two slab waveguides. The horizontal lines represent the interfaces between the core and the cladding. The direction of propagation can be taken from left-to-right (or vice versa). Also, the beat length is given by the horizontal lines.

2.7 Theory of Optical Microresonators WGM

Optical microcavities recently are becoming very important photonic blocks in a variety of applications. One of the fundamental device that uses principles of light cavity are whispering gallery modes. WGM are some specific resonances (Eigen) modes of wave field in inside of a given resonator, or cavity. The waves which are coupled into the cavity, they circulate around it, owing the phenomenon of total internal reflection. In this sense, they reach the resonance condition and after one round-trip they achieve the same position and return in the same phase (modulus 2π), where they also interfere constructively with themselves, from where the form the standing waves. Geometry of the microresonator plays a key role on the resonance effect [18].

WGM, is a classic device of a light microcavity, as a term was introduced for the first time by Lord Rayleigh in the 19th century to describe some gallery whispering phenomena located inside of the dome of the Saint Paul cathedral, in England. A sound that was propagated in a point of the dome, could be heard in the opposite part, a considerable distance away from the source. Lord Rayleigh analyzed this phenomenon by warning that the sound remains to the walls of the dome and circulate only within a narrowed layer close to the concave part of the gallery (Fig 2.8). The intensity of a propagated sound decays only in direct proportionally to the distance of from the source, comparing

FIGURE 2.9: A picture from the inside view of the dome of the Saint Paulâs Cathedral, and a schematic representation of whispering gallery for that dome [21].

to free space at which the intensity decreased equally to the square of the distance from the source. Thus, in WGM is slower rather in free space, which give us the possibility to hear loudly even in a large distance out of the source. This interesting sound effect was named as Whispering Gallery Mode [20].

Additionally, the beginning of the 20th century has shown a significant interest due to the fact of existing of electromagnetic waves in dielectric spheres that had nearly the same effect and structure as acoustic whispering gallery mode. Despite it took almost a century until 90s years of last century to bring into the 'life' any real device application (see Figure 2.11 [6, 12].

2.7.1 Parameters of Optical Resonators

In order to have some estimation mechanisms for general considerations regarding to theory and implementation of optical resonators, we are going to analyze some parameters that in a form or another affect the performance of these devices. Some of them are: Quality factor, Loss mechanisms, Finesse and Mode Volume.

2.7.1.1 Quality Factor (Q)

Quality factor is a dimensionless parameter that includes the energy losses inside any resonant component modified in any mechanical pendulum, optical resonator, or any resonant electronic circuit, such as RF circuits [22]. This parameter represents one of the most important mechanism to describe the performance of wave resonations, and consist of [23]

$$Q = \omega_0 \times \frac{Energy\ Stored}{Power\ Loss} = \omega_0 \tau = \frac{\omega_0}{\triangle\ \omega_{FWHM}}. \tag{2.31}$$

From the last expression: $\omega_0 = 2\pi\nu_0$ is the angular frequency. ν_0 is the resonance frequency, τ represents the cavity ring down lifetime, which is the time necessary for the intensity of the field to decrease by a factor of e and $\triangle \omega_{FWHM} = \tau^{-1}$ is the linewidth of the 'uncertainty' for the frequency of the resonance (full-width-at-maximum of any resonance peak or FWHM) in angular frequency.

In many applications, such optical resonators, a high Q factor is crucial. Usually, we refer as high Q-factors from around 10^3 to 10^6 as high Q-factor elements, and those with 10^7 and higher, as ultra-high Q-factor [24].

Another way of interpreting this parameter is whole energy circulating modes within a resonator at equilibrium, divided by energy that has to be pumped in to the resonator in the time of one full field oscillation, times 2π , to maintain the equilibrium. This is for a higher Q-factor of the intensity of total field or total energy stored inside the resonator, of the circulating mode is proportionally higher at the same pumping power. Recently, beyond all physical nonlinearities, some ultra-high Q- factor of some optical resonant devices can maintain the circulating intensities to reach an extremely high values, even

with a moderate power of pumping (milliwats) which lead us to a simplification of the study and to a higher efficacy of these devices [25].

The other way of expressing the quality factor is by circulating mode from the complex propagation constant or in wave number: $k_{0,\epsilon} = \frac{\omega_\epsilon}{c_0} = \beta + \frac{1}{2} \times i\alpha$. For $\beta = \frac{2\pi}{0}$ is the phase constant and is element of real numbers. λ_0 is wavelength in vacuum and α represent the the intensity of attenuation coefficient for the various cavity mechanism [26]:

$$Q = \frac{\beta}{|\alpha|} = \frac{Re(\omega_\epsilon)}{2|Im(\omega_\epsilon)|} \tag{2.32}$$

2.7.1.2 Loss Mechanisms

The original Q-factor takes contributions due to the losses from many real-world reasons and in a way can be written as:

$$Q_{int}^{-1} = Q_{mat}^{-1} + Q_{surf}^{-1} + Q_{scatt}^{-1} + Q_{bend}^{-1} \tag{2.33}$$

The pure original Q-factor is known also as intrinsic (Q_{int}), Q_{mat} represents the absorption of material, Q_{surf} is absorption losses of surface in the case of coatings or absorbing material such as the surrounding material around the microresonator and is the bending loss in resonator or radiation loss.

For illustration we can refer to the example of silica (SiO_2) for $\lambda_0 = 1.55\mu m$ to scattering losses in the vacuum wavelength of minimum loss for a bound of absorption, limited by Q-factor $Q_{abs} = \frac{2\pi n}{\alpha_0} \approx 3 \times 10^{10}$ [15]. In this expression n is the refractive index of silica and is the coefficient of intensity attenuation [27].

Total internal reflection is one of the main contributors towards optical resonator losses due to the fact that a curved interface is never completed and it leads to a transmitted wave in a lower refraction index. Resulting in energy spread off to the resonator. The resulting quality factor shows a significant dependence to resonator radius for a constant given resonance wavelength. For illustration let us consider the sphere: $Q_{bend} \approx e^{4\pi n \frac{\alpha}{\lambda_0}}$, thus, in this expression - is the radius of the sphere [28].

For cases when cavities in which the light is provided via an external waveguide with total internal reflection (as in our study), quality factor is exposed to another loss contributor called external(Q_{ext}), and in general form of Q-factor is related by the following expression:

$$Q_{tot}^{-1} = Q_{int}^{-1} + Q_{ext}^{-1} \tag{2.34}$$

2.7.1.3 Finesse($\mathfrak{F}$)

Finesse is another parameter for characterizing a resonatorâs performance. For finesse approximation, usually a high range is desirable. Definition of this parameter is simply as a ratio of the free spectral range $\triangle \nu_{FSR} = \frac{\triangle \omega_{FSR}}{2|pi}$, in a side and FWHM linewidth resonance [23]

$$\mathfrak{F} = \frac{\triangle \omega_{FSR}}{\triangle \omega_{FWHM}} = Q \times \frac{\triangle \omega_{FSR}}{\omega_0} < Q. \tag{2.35}$$

In fact, finesse of a resonator provides us information related to the distance between the resonance peaks in terms of the number of FWHM linewidth which goes between a couple of resonant peaks. Comparing with the Free Spectral Range which describes the distance between the peaks in absolute value terms. Based on this fact that resonant frequency/wavelength are in general around equally distinguished, a resonator interferometer can only separate between frequencies that takes part in inside of any period of length FSR. That is basically the main reason why an optical resonator we call fully tunable due to the fact that it can be tuned over and over of free spectral range. Finesse is a parameter which is also related to quality factor. This is realized by equating quality factor and multiplying to the fraction of the spectrum in a resonant frequency, covered by any free spectral range of the resonator. For this reason, finesse always is equally to or less than 1. Therefore, finesse gives information about the effective resolution of the resonator as an interferometer (number of different frequencies that it can be distinguish) [25].

2.7.1.4 Mode volume

The last parameter that we are going to discuss over here is mode volume. Mode volume of any field for a Eigen-mode of a resonator is defined as the ratio of the whole stored

energy inside the resonator and the maximum density of that mode:

$$V_{eff} = \frac{StoredEnergy}{Max.EnergyDensity} = \frac{\int_\mu w(r)d^3r}{max(w(r))} \tag{2.36}$$

In electromagnetic field: $w(r) = \frac{1}{2}(\epsilon_0\epsilon(r)|\vec{E}(r)^2 + \frac{1}{\mu_0\mu(r)}|\vec{B(r)}|^2)$, where ϵ_0, $\epsilon(r)$ represent the total electric permittivity and $\mu_0, \mu(r)$ - the total magnetic permeability. There is e correlation between mode volume and free spectral range. This relation is inverse proportionally, thus, lower mode volume leads to a higher free spectral range. It is also related to lasing characteristics of a resonator due to the fact that contains a lasing medium. This is related with spontaneous emission rates that is inversely proportional. Another specification for mode volume is that the minimum limit for lasing effect is directly in dependence from the mode volume and consequently a small module volume is desirable [29].

2.8   Theory of Ring Resonators

The basic configuration, as previously mentioned is composed by unidirectional coupling between a ring-shape waveguide with radius r and a straight-form waveguide, as shown in Figure 2.9. By assuming that a single unidirectional mode is excited, the coupling is lossless, considering a single polarization. Many lossless effects occur along a light propagation within the ring resonator which are include in the attenuation constant [3]. The relation can be described by the following matrix expression:

$$\begin{pmatrix} E_{t1} \\ E_{t2} \end{pmatrix} = \begin{pmatrix} t & \kappa \\ -\kappa^* & t^* \end{pmatrix} \times \begin{pmatrix} E_{i1} \\ E_{i2} \end{pmatrix} \tag{2.37}$$

The complex mode of amplitudes E are normalized; hence, their squared magnitude corresponds to the modal power. and t, represent the coupling parameters and they depend on the specific coupling mechanisms used. The '*' symbol denotes the conjugated complex value of t and κ factors.
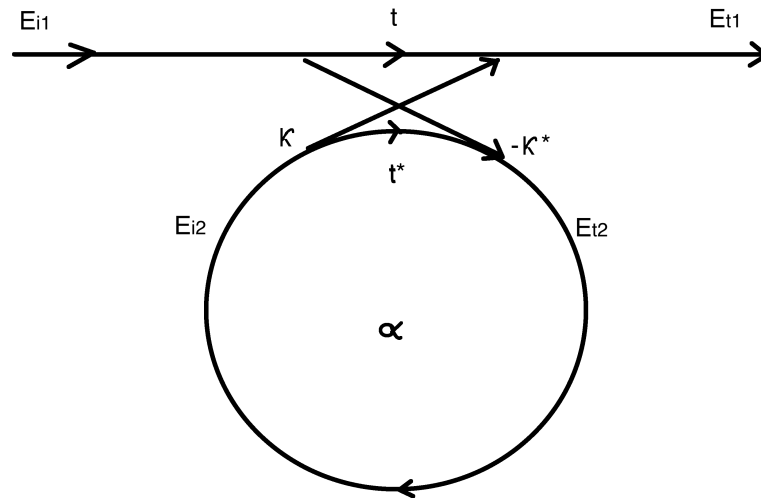
FIGURE 2.10: Model of a single ring resonator with one waveguide

For this case, the matrix is symmetric because the elements under consideration are reciprocal. Thus,

$$|\kappa^2| + |t^2| = 1. \tag{2.38}$$

For a further simplification, E_{t1} is equal to 1. Then the round trip in the ring is given by

$$E_{i2} = \alpha e^{j\theta} E_{t2} \tag{2.39}$$

where: α is the loss coefficient of the ring (if zero loss then $\alpha = 1$) and $\theta = \frac{\omega L}{c}$, L is the circumference of the ring that is given by $L = 2\pi r$, r - represents the radius of ring measured from the center of the ring to the center of waveguide, c - is the phase velocity of the ring mode ($c = \frac{c_0}{n_{eff}}$, fixed angular frequency $\omega = kc_0$, and c_0 constant refers to the vacuum speed of light. The vacuum wavenumber k is related to the wavelength λ via: $k = \frac{2\pi}{\lambda}$. Using the vacuum wavenumber, the effective refractive index can be expressed into the ring coupling by

$$\beta = k\eta_{eff} = \frac{2\pi n_{eff}}{\lambda} \tag{2.40}$$

and β is the propagation constant. Then

$$\theta = \frac{\omega L}{c} = \frac{kc_0 L}{c} = k2\pi r n_{eff} = \frac{2\pi n_{[eff]}}{\lambda} = 4\pi^2 n_{eff}\frac{r}{\lambda} \tag{2.41}$$

By Equation 2.37, Equation 2.1 and Equation 2.39 we obtain

$$E_{t1} = \frac{-\alpha + te^{-j\theta}}{-\alpha t^* + e^{-j\theta}}, \tag{2.42}$$

$$E_{i1} = \frac{-\alpha\kappa^*}{-\alpha t^* + e^{-j\theta}}, \tag{2.43}$$

and

$$E_{t2} = \frac{-\kappa^*}{1 - \alpha t^* e^{j\theta}}. \tag{2.44}$$

After this we can derive the transmission power P_{t1} in the output waveguide, which is

$$P_{t1} = |E_{t1}|^2 = \frac{\alpha^2 + |t|^2 - 2\pi|t|\cos(\theta + \varphi_t)}{1 + \alpha^2|t|^2 - 2\cos(\theta + \varphi_t)}, \tag{2.45}$$

where $t = |t|exp(j\varphi_t)$, $|t|$ represent the coupling losses and the coupler phase. In the other side, circulating power P_{i2} in the ring is given by

$$P_{i2} = |E_{i2}|^2 = \frac{\alpha^2(1 - |t|^2)}{1 + \alpha^2|t|^2 - 2\cos(\theta + \varphi_t)}, \tag{2.46}$$

When on resonance,$(\theta + \varphi_t) = 2\pi m$, m- is an integer, and in following step is obtained

$$P_{t1} = |E_{t1}|^2 = \frac{(\alpha - |t|)^2}{(1 - \alpha|t|)^2}, \tag{2.47}$$

and

$$P_{i2} = |E_{i2}|^2 = \frac{\alpha^2(1 - |t|^2)}{(1 - \alpha|t|)^2},$$

(2.48)

Special case is when $\alpha = |t|$ the transmitted power becomes zero, and this corresponds to Equation 2.47. In literature is knows as critical coupling, and occurs because of destructive interference or light losses, in terms of transmitted to the output. By combining the above equations, we can have a visualization of the basic configuration with only a ring and a straight waveguide, and its behavior will looks like in the following graph.
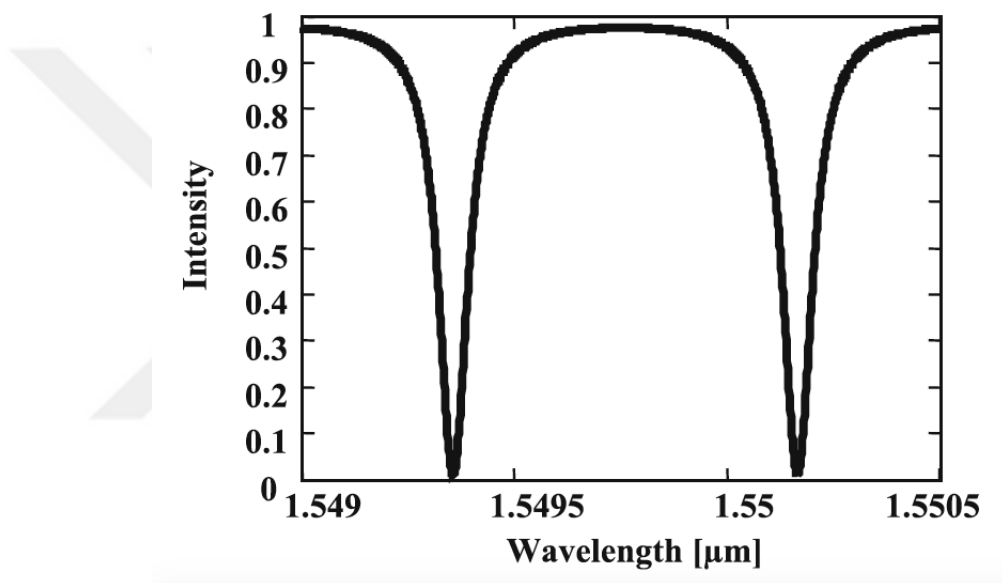

FIGURE 2.11: Notch type ring resonator characteristics

In conclusion, this chapter deal about general theoretical concepts about optical dielectric waveguides as well sa optical microresonators. Their importance lies in many bases that are related to optical resonators.

Chapter 3

Results and Discussions

3.1   Nanoparticles Sensing

Clinical diagnostics mostly rely on sensing molecular nanoparticles based on biochemical assays like enzyme-linked immunoassays (ELISA), radiolabeled immunoassays, or polymerase chain reactions (PCR). Other detection techniques include the usage of biorecognition elements such as antibodies or similar bioagents [30]. All of these diagnostic methods need chemical amplification as well as labeling of the analyte in order to give any detectable signal. They require biochemical and physical requirements by following many procedures. Moreover, the ways of analyzing require adequate and trained professional workers [1]. Therefore, it will be too costly to have a well-equipped laboratory with all the needed. For most of the reasons above, there is a need for real-time, portable and cost effective analyzing techniques especially in healthcare sector [2, 9]. In this way, one of the serious candidates for a micro âworldâ biodetection is optical microring resonator [31]. Small array usage makes the fabrication on small chips possible. This in turn helps in doing mass production and makes the cost of production low [19].

3.2   Correlation between the Ring Radius Variation and Resonance Shift as Sensing Mechanism

In this thesis work, an optical micro-ring-based resonator is used to develop a simulation-based model using multiphysics finite element method. This model is developed by

using COMSOL Multiphysics software tool. An input tunable laser light at the input node of the straight-form waveguide at a wavelength of 1.55 μm was applied, and the transmitted light at the output node was monitored. Refraction index for the *core* layer and *cladding* of the resonator fiber was set to 2.5 and 1.5 respectively. According to the obtained results, a linear correlation between increasing the radius of the microring and the red shift in the existing wavelength resonances was observed. Figure 3.1 shows a representation schematic of a microresonator and its biosensing principle of work [32].
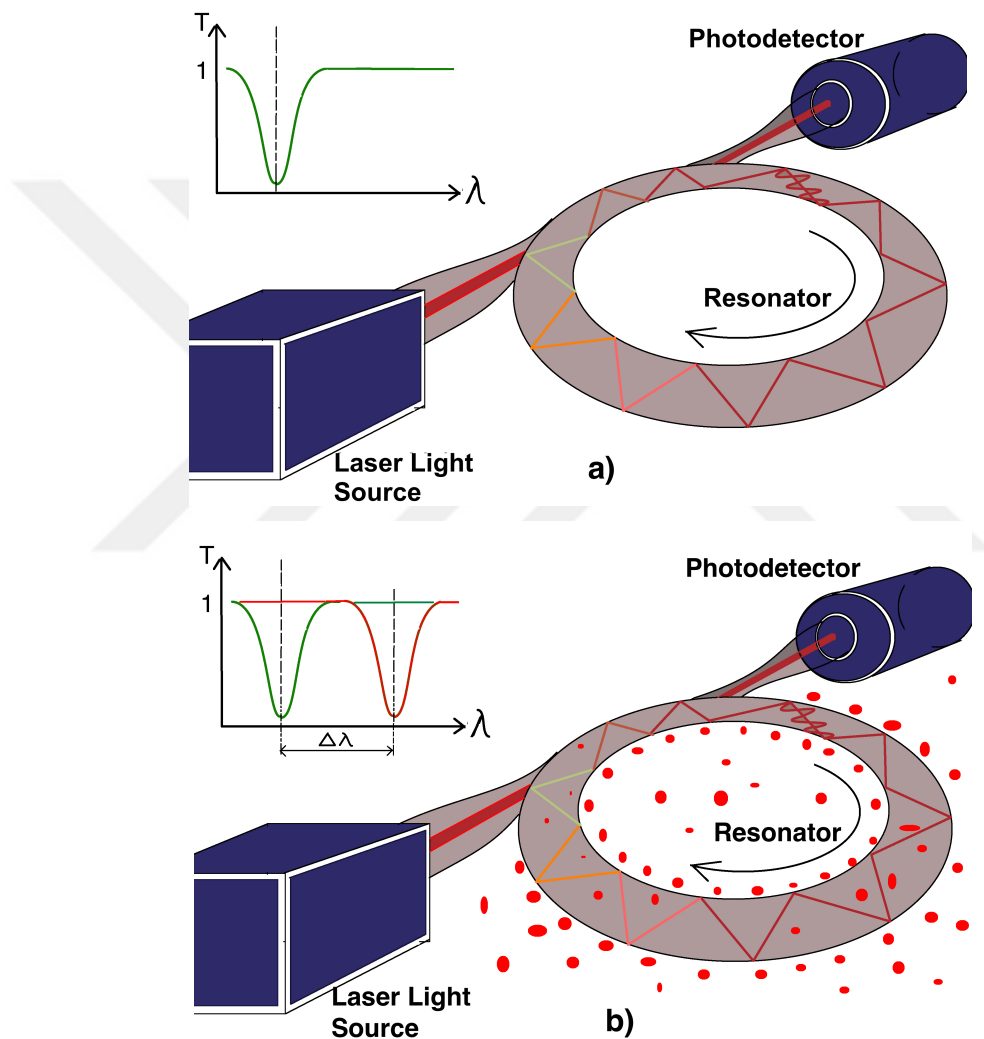

FIGURE 3.1: A schematic for representation of microresonator biosensing principle of work

The figure contains a laser light source, a tapered fiber, a ring-shaped resonator, and a photodetector. Figure 3.1a) shows a possible setup for a resonator operation before putting in any analytical process. In the graph, the transfer function indicates the transmittance (T) and the minimum Lorentzian line (transmission peak) with an arbitrary

location at the abscissa. One can determine the resonance wavelength of this optical ring micro-resonator by sweeping the wavelength of a waveguide-coupled by tunable laser source. The transmission spectrum can be monitored by photodetector which is posiotioned at the output of the fiber. When it reaches the resonance state, it can be seen that the lowest value of the Lorentzian line is shifted by $\Delta\lambda$ after the biomolecules are added. This shift is utilized as a parameter for sensing mechanism.

Additionally, it was found that we can detect resonance shift for very small changes in micro-ring radius, as low as $10nm$. In this manner, it is assumed that biomolecules are attached to the ring and the graph of transmission function with respect to resonance shift ($\Delta\lambda$) is displayed. Also, it is assumed that nanoparticles size is much lower than the thickness of the resonator ring and when they are around the ring, they act like a monolayer structure. This resonance shift can be detected as is shown in Figure 3.1 b) in the upper-left graph, which is illustrated with the red line.

By increasing the accumulation of bound molecules, it will reduce the intermolecular splitting distance and then its size becomes comparable to the light wavelength. Eventually, an optical closed monolayer is created which causes an extension for merging, in both sides of the ring. Consequently, the wave function follows a circular orbit with a larger radius. In this manner, it can be modeled as nanosized monolayers around the resonator with the aim to mimicks the material of biomolecules. All of the process is realized by assuming the refractive index (RI) of the microring resonator and RI of the biomolecules will be homogenous. Based on this approximation, the reactive resonant shift in wavelength coordinate was monitored. Accordingly, the maximum monolayer density of the dielectric properties to the accumulated biomolecules and the ring material will be equivalent [30]. From the optical point of view, this dielectric ring resonator is grown in thickness.

The model with different size of thickness of the layer around the ring is simulated. Simulation starts from $10nm$ and is then increased to $20nm$, $30nm$,..., and so forth until$200nm$. This process is performed in order to characterize the size of mimicked bimolecules that is supposed to be detected.

Figure 3.2 shows the variation of the electric field inside of the resonator. Gradient colored bar in the right side denotes the values for the electric field, from the negative and positive range. The width of both vertical and circular fibers is 2 μm. The light

wave circulates to the larger ring radius (R), which in this case is R=83.00 μm, and a wavelength of $\lambda = 1.550 \ \mu m$.
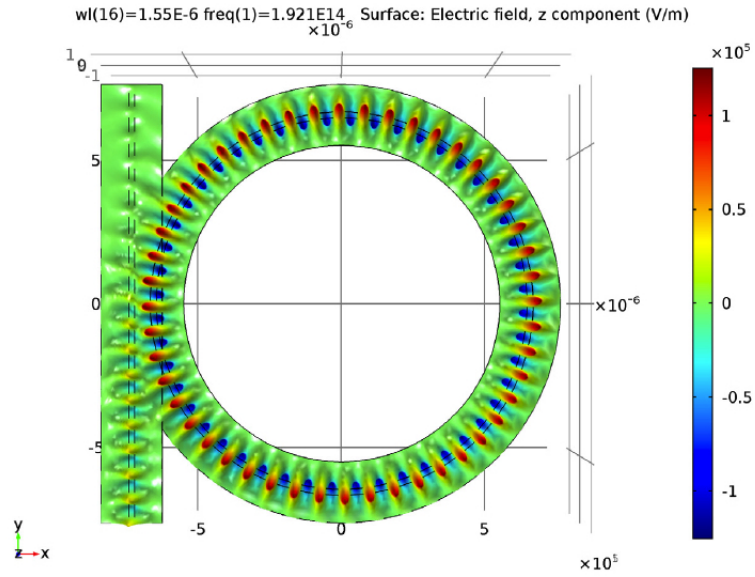

FIGURE 3.2: The out-of-plane component of the electric field for the resonant wavelength.

The bottom part of the vertical waveguide represents the source of tunable laser light, which is labeled as Port 1. The other end is labeled as Port 2 and the transfer function of the transmitted light is monitored at this position.

Condition to reach the resonance effect is given by

$$\frac{m\lambda_R}{n} = 2\pi R. \tag{3.1}$$

Where n represents refractive index (RI) of the ring, m is an integer number for orbital wavelength. From this expression, it is obvious that any change in either the radius (R) or in the effective refraction index (n_{eff}) of the optical mode will impact the wavelength that satisfies the condition of the resonance effect (ΔR).

Equation 3.1 states that the changes of the resonance wavelength caused by the changes in radius ΔR. The impact can be seen more clearly from the below expression

$$\frac{\Delta \lambda_r}{\Delta \lambda_r} = \frac{\Delta R}{R} + \frac{\Delta n_{eff}}{n_{eff}}. \tag{3.2}$$

Increasing the radius of the ring leads to a red shift in the position of the impacted resonance wavelength. This enhances the hypothesis that any small change in effective refraction index (RI_{eff}) must be balanced by an equally small shift in the resonance wavelength. Also, here obviously can be seen that the behavior of this resonance shift is the fundamental parameter on the sensing process.

To use this resonator as a sensor, the values of resonance shifts needs to be quantified in a linear trend. In another words, when we look at the wavelength coordinate those values are going to be positioned successively, with respect to its position value in the x-coordinate. Measurements are realized by monitoring the transmitted light intensity passing through the straight waveguide. After the light propagation around the ring, some light couples back to the straight waveguide and interferes with the incident light. At the resonance state, a completely destructive interference can be obtained at Port-2, with no any transmitted light. Therefore, these characteristics make an optical ring resonator an ideal sensor by monitoring the light intensity at the resonant wavelength. Another advantage is that can be used in real time.

In this thesis work, one of the challenging parts has been the determination of an adequate ring radius. The term adequate radius is the resonator having linear response. There have been many tests required to reach that level of response. The tests have started with radius of 20 μm, and then increased to 30 μm, 40 μm, and so forth, until around 200 μm. Most of the responses from the simulations did not match the criteria to provide a linearly successive response in order to quantify those values in linear trend. Then these values are to be used in characterizing the size of the layer. Interestingly, it was found that these successive responses for the respective resonant wavelengths can be acquired, in a range between 80 μm and 90 μm. It started to give a linearly scaled responses with every 0.5 μm increment from a range between $83\mu m$ and $85\mu m$ (see Figure 3.3). Radius changes need to be more narrowed, and then has to be continued by the changes between 83.00 μm and 83.10 μm, with an increment rate of $10nm$. By this model, we could obtain information that can help to specify the size of bind nanoparticles around

the ring. Nanoparticles in this model are represented by the extended thin layer (the layer thickness).

The resonance wavelength shift depends sensitively on changes on the optical length path of the travelling light in a linear trend. This effect occurs due to the binding of biomolecules around the micro-resonator at outer part of surface (molecules positioned at the vicinity of the ring) which in fact increase the thickness of the ring.
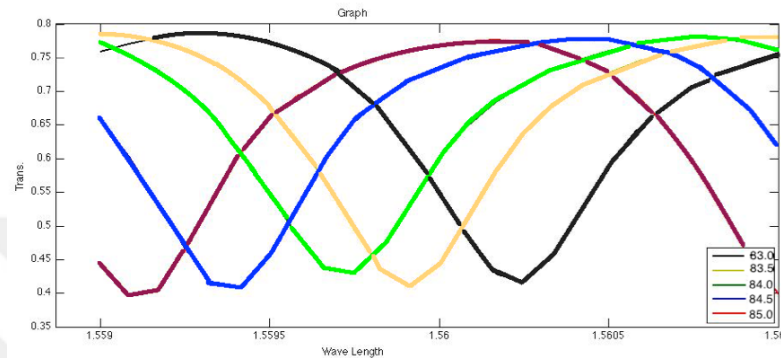

FIGURE 3.3: Linear successive responses, compiled for the simulations of the microresonator by varying the ring radius, starting from 83 μm to 85 μm.

In Figure 3.3, the responses are compiled for the range values 83.00 μm, 83.05 μm,84.00 μm, 84.05 μm and 85.00 μm. This data compilation is performed using Matlab software tool. Later, the same graph is used to read values of the spectrum in order to locate the exact minimum position, based on different colored lines. These lines correspond to the exact resonance wavelength position of the resonator response. The same procedure is followed for more increments between these values (see Figure 3.4) [32].
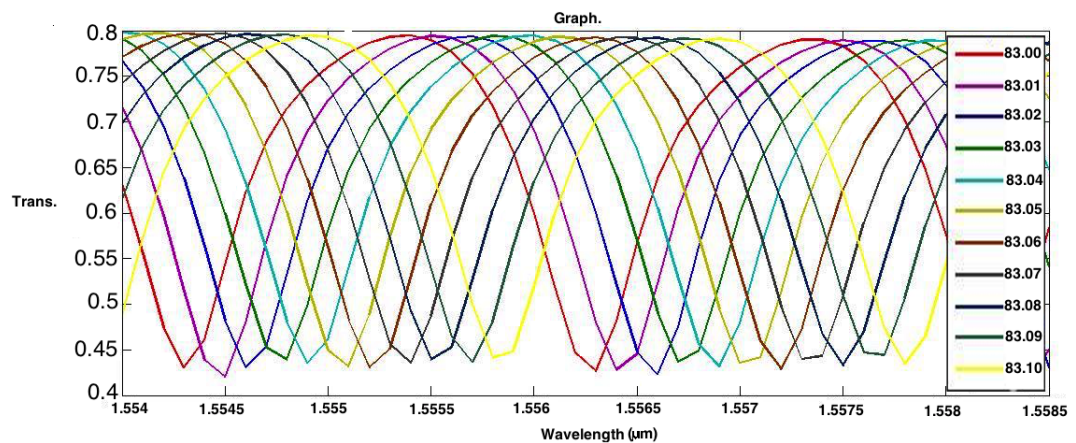

FIGURE 3.4: Linear successive responses, compiled for the simulations of the microresonator by varying the ring radius, starting from 83.00μm, 83.01μm, 83.02μm,â, 83.10μm. The measurement is performed by tuning a laser near one of the resonances of the ring and detecting the change in the spectrum.

From Figure 3.4, the exact resonant position can be determined, which has been started from the first resonance value (red line). Wavelength of 1.5543 μm corresponds to the first resonance in the first model, or 1.5563 μm on second part of modes. The binding nanoparticles are assumed to be in size of $10nm$ and they are approximated as straight layers that cause a resonance shift. First mode wavelength shift corresponds to value of 1.5545, or 1.5565 μm for the second mode. This resonance wavelength shift continues to be increased sequentially in a linear fashion for every single time we increased the width of the ring by an increment of $10nm$ in both sides of the ring. For instance, the last resonance shift in the same figure consists of a shift which is caused by biomolecules of the size of $100nm$. The corresponding resonance wavelength value for this case is 1.5559 μm or 1.5579μm second mode. Another characteristic for this graph is the resonance amplitude of the transmitted light, which in this case happens to be from 0.8 to around 0.4.

Figure 3.5 shows a way of data presentation from Figure 3.4, which represents the resonance shift as function of the thickness of the resonator. In the beginning, the shifting curve starts from zero. Then, it can be observed that for a layer size around 10 nm causes a shift of $0.4nm$. The simulation can be performed for all the sizes of the extended layer, but only 3 cases have been displayed in this graph. The second case has the shift value of $1.9nm$ and 40 nm is the corresponding layer size. The largest value which is shown in this graph has 100 nm layer thickness and consequently shift of 3.4 nm [33].
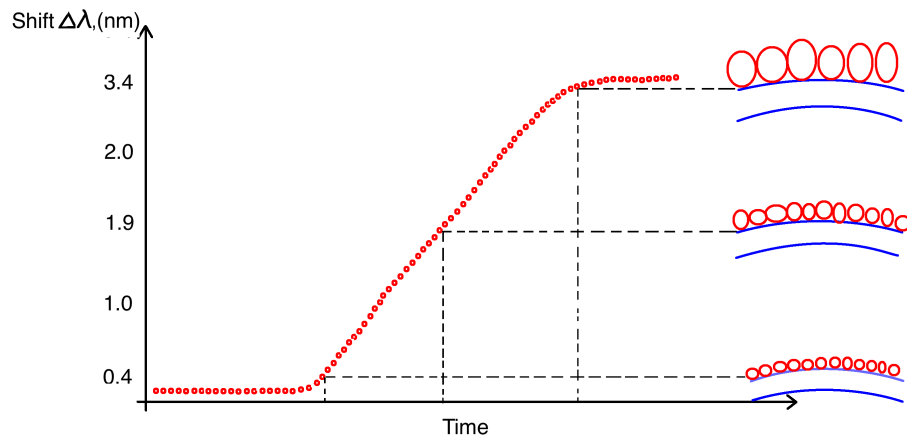

FIGURE 3.5: Evaluation of sensitivity in function of the layer thickness

Simulations revealed that the same trend continues for higher values of the ring thickness. Simulations are performed until value of $220nm$, as shown in Figure 3.6. The only

difference between Figure 3.5 and Figure 3.6 is relies in the transmitted light intensity that has slightly gone towards minimum values. All the radius responses can be read from the graph when it is plotted. However, Figure 3.6 are shown with data from $R = 83.11\mu m$ until radius value of $R = 83.22\mu m$.
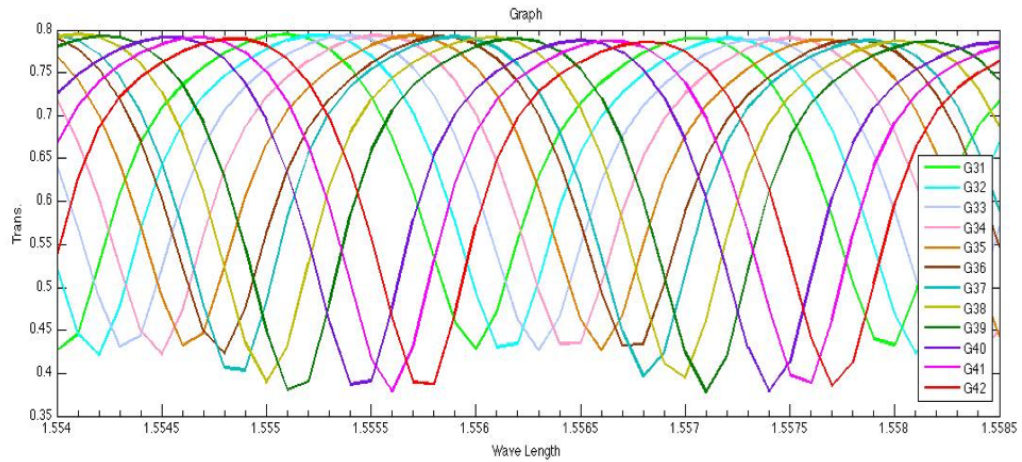
FIGURE 3.6: Resonance shift for radius 83.11 μm to 83.22μm

As for illustration, a direct plot for a random simulation on COMSOL Multiphysics can be seen from following Figure 3.7.
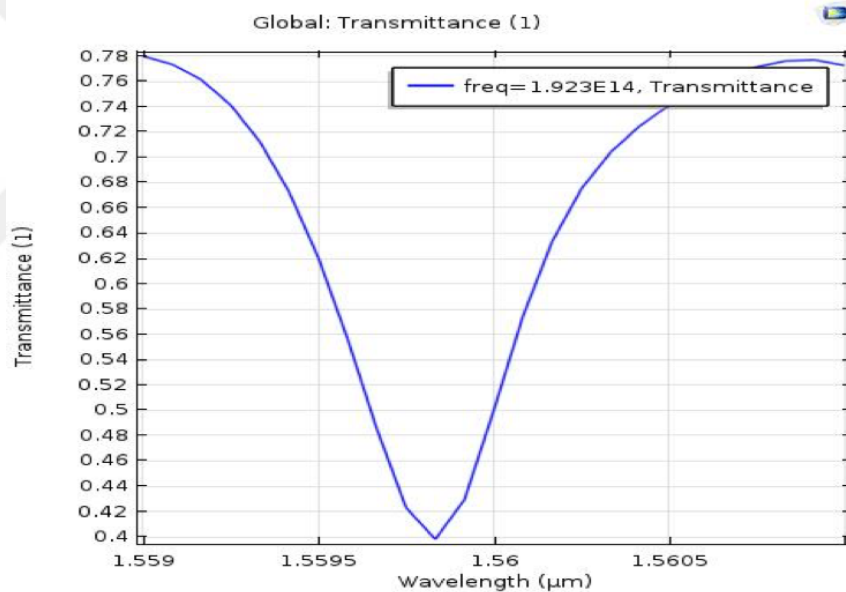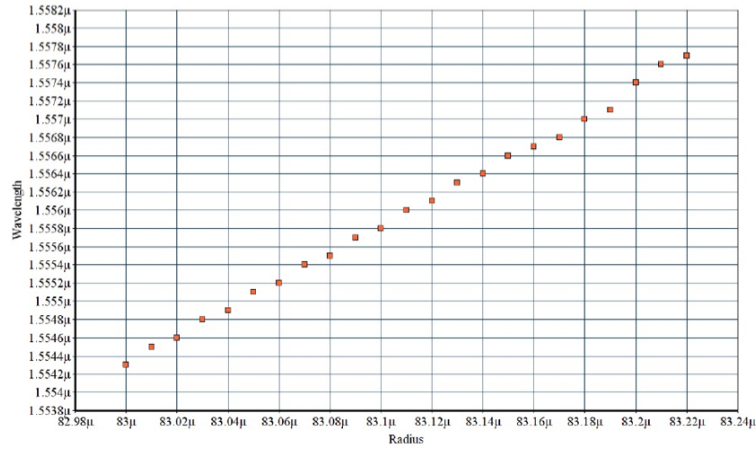

FIGURE 3.7: Transmittance of the light as a function of wavelength. The sharp dip shows transmitted light intensity drop (resonance wavelength peak)

In order to have a full picture for all the shifts for the outer ring radius values of 83.00 μm to 85.20 μm, all the data are collected and compiled in a single graph in Figure 3.8.

FIGURE 3.8: Resonance shift for radius 83.0μm to 83.23μm

3.3 Q factor, Transmittance as a Function of Distance Between the Waveguides, FSR and FDHW Parameters Optimization

This section refers to the operation and performance of the micro-resonator itself. The model is explored out to have a clearer picture that will help in ring resonators principle of work and their parameters performance. An interesting characteristic consists of the fact that when the diameter of the ring is increased, it causes a decrease in the Free Spectral Range (FSR) parameter. FSR denotes the distance between two successive resonances. Figure 3.9 shows a typical transmission spectrum of a ring resonator with radius of 60 μm. In the simulations is to be positioned in a free medium. For 60 μm resonator radius, the Q factor was calculated $15.5 * 10^6$ at a resonant wavelength of $1550nm$, and approached round-trip loss of 10%. The corresponding full width at half maximum (FWHM) was 0.3 nm and the free spectral range is $2.8nm$. The resonance amplitude for this transfer function varies between maximum 0.8 and a minimum value of 0.43.
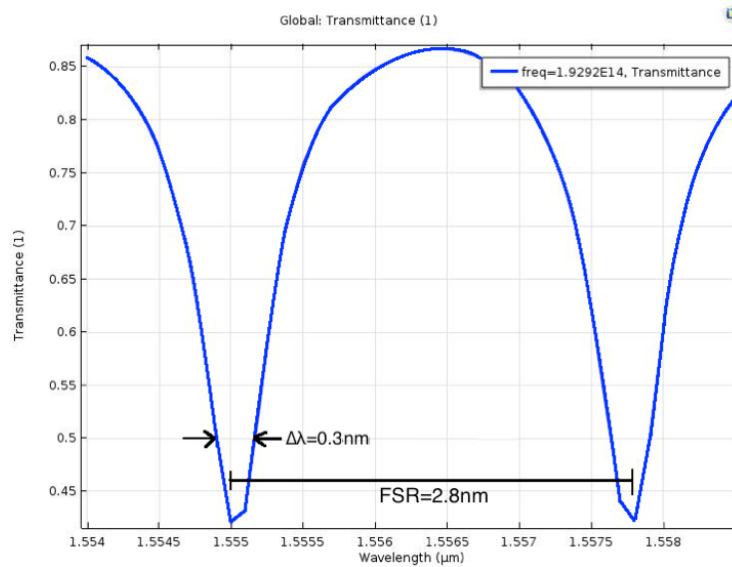
FIGURE 3.9: Response for resonator ring radius 60 μm and its FSR value of 2.8 μm

Figure 3.10 shows the spectrum for a ring radius of 80 μm. In this case, the Q factor was $20.2 * 10^3$, at a wavelength of 1550 nm and approached a round trip-loss of 10 %. FSR for this case is $2.1nm$ and is smaller than the previous case for $0.7nm$. The corresponding full width at half maximum is $0.3nm$. The spectrum resonance amplitude was between value of 0.81 and 0.42.
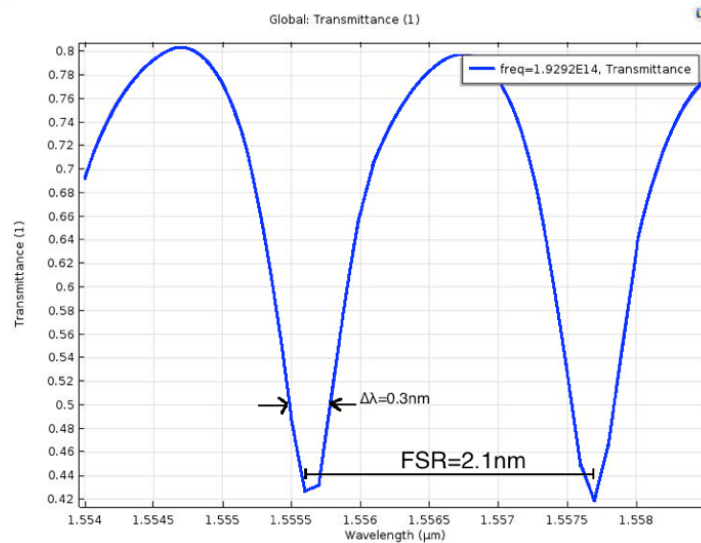

FIGURE 3.10: Response for resonator ring radius 80 μm and its FSR value of 2.1 μm

For resonator ring radius of 100 μm Q factor was $25.4 * 10^3$, with the same percentage of the round-trip loss approximation, 10%. FSR for this spectrum corresponds to $1.6nm$ and FWHM was $0.35nm$. Comparing to the previous case, it is a difference of $0.5nm$ in parameter of FSR and a $0.01nm$ difference in the FWHM. This spectrum is shown in

following Figure 3.11. The minimum and maximum values for the resonance amplitude varies between 0.79 and 0.42.
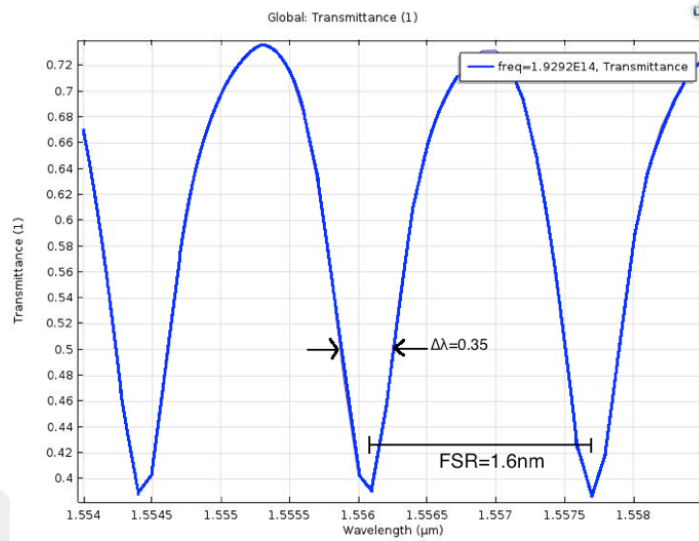

FIGURE 3.11: Response for resonator ring radius 100 μm and its FSR value of 1.6 μm

The last case that was studied towards optimization of some of the resonator parameters consists of a 120 μm outer ring radius. Spectrum for this transfer function is shown in Figure 3.12. The Q factor was $30.6*10^3$ at a wavelength of $1550nm$. Corresponding FSR is $1.3nm$, and FWHM of $0.4nm$. Comparing to the previous case, there is a difference of $0.3nm$ for the FSR characteristic. For FDHM parameter, there is a difference of $0.05nm$. Corresponding resonance amplitudes were between 0.67 and 0.36.
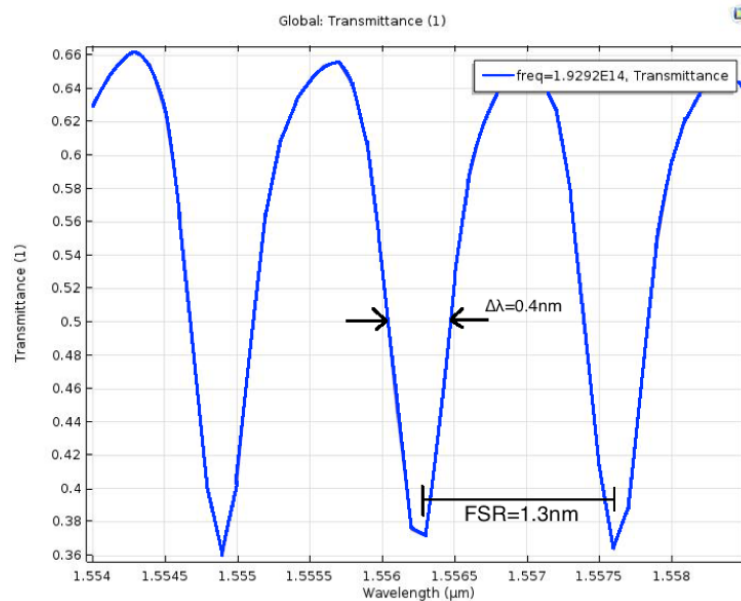

FIGURE 3.12: Response for resonator ring radius 120 μm and its FSR value of 1.3 μm

Conclusively, for the last four cases of resonator ring size, it was found that the amplitude of the resonance was proportional to the size of the resonator rings. With increase in the radius, the resonance amplitude range is increased (Figures 3.9-3.12). Also, by increasing the size of the ring it almost linearly decreased the FSR characteristic, but a slightly decreased the FDHM.

Figure 3.13 shows a plotted data graph for FSR as function of the ring size, for radius of 60.00μm, 80.00μm, 100.00μm and 120.00μm respectively.
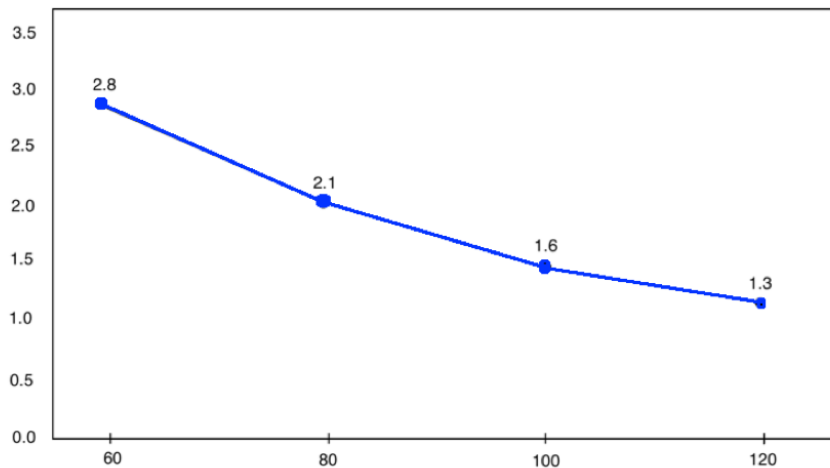

FIGURE 3.13: Distance between the resonances peaks (Free Spectral Range -FSR) as function of ring radius

The following figures are plotted with the data which reveal information about the linear variation of the ring size. The tests have been started with an increment of $10nm$ from radius $60.00\mu m$ to $60.10\mu m$, $80\mu m$ - $80.10\mu m$, $100\mu m - 100.10\mu m$ and $120\mu m - 120.10\mu m$. These data are plotted in following Figures 3.14 - 3.17. A correlation between the increasing the ring radius and the wavelength red shift is observed. Figure 3.13 shows the value of this ring size and wavelength increasing in a linear trend for radius $R = 60.00\mu m$, $R = 60.01\mu m$,...,$R = 60.10\mu m$.

Figure 3.15 shows simulation results that have been plotted for resonance shift as a function of wavelength, and ring size correlation for radius of $R = 80\mu m$. Here also, a $10nm$ increment is applied.

The last concept that is studied regarding to the resonator performance and optimization is the coupling effect. This phenomenon occurs between the waveguides and the ring itself. Some suggestions are given related to the distance between the straight waveguide and the ring-form waveguide. It is worthwhile mentioning here that the parameter of light
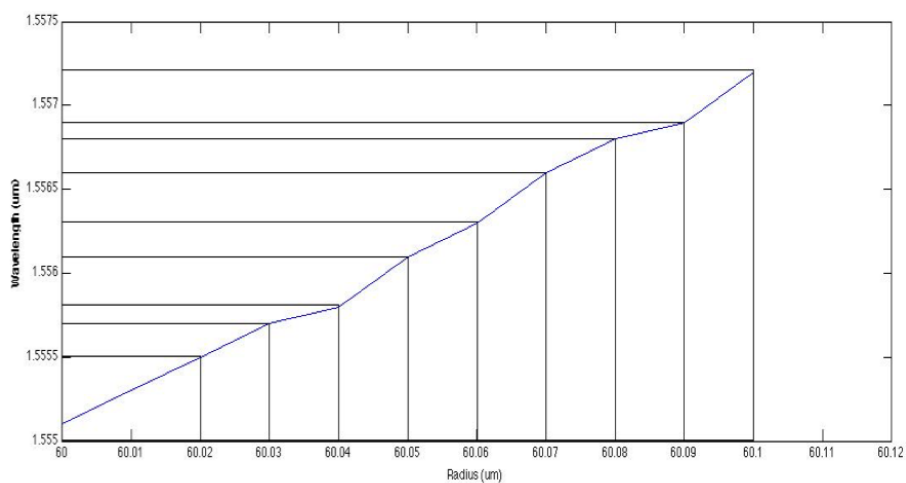
FIGURE 3.14: Resonance shift for ring radius 60.00 μ m increasing by an increment of 10 nm until 60.10 μ m.
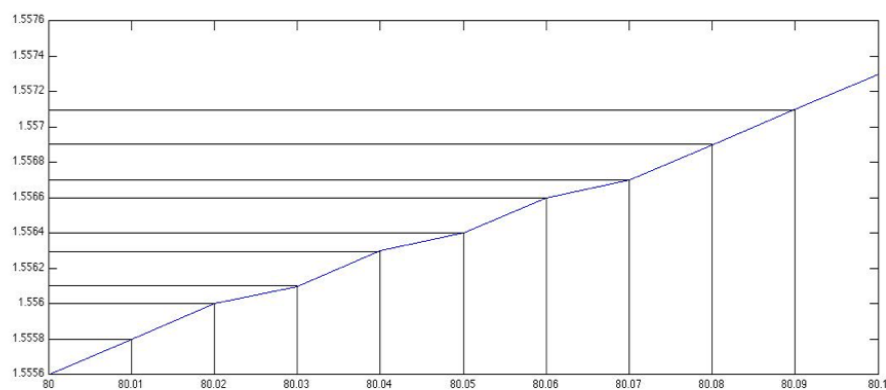

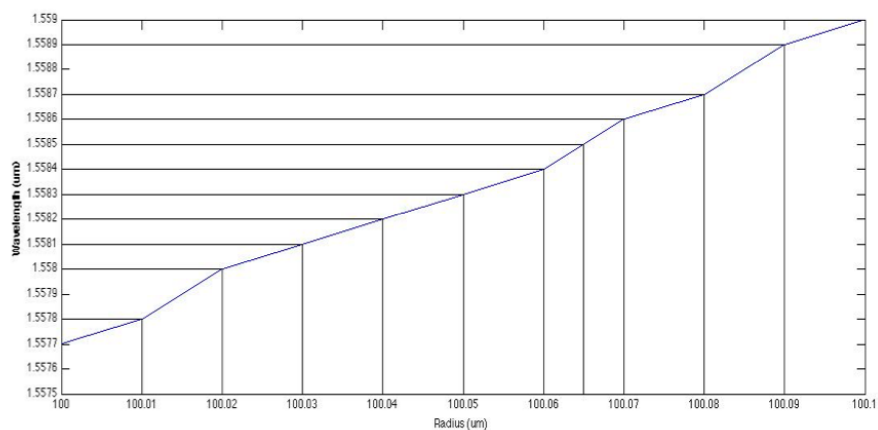FIGURE 3.15: Resonance shift for the ring radius increasing started from $80.00\mu m$ to $80.10\mu m$

FIGURE 3.16: Resonance shift for ring radius 100.00 μ m increasing by an increment of 10 nm until 60.10 μ m.
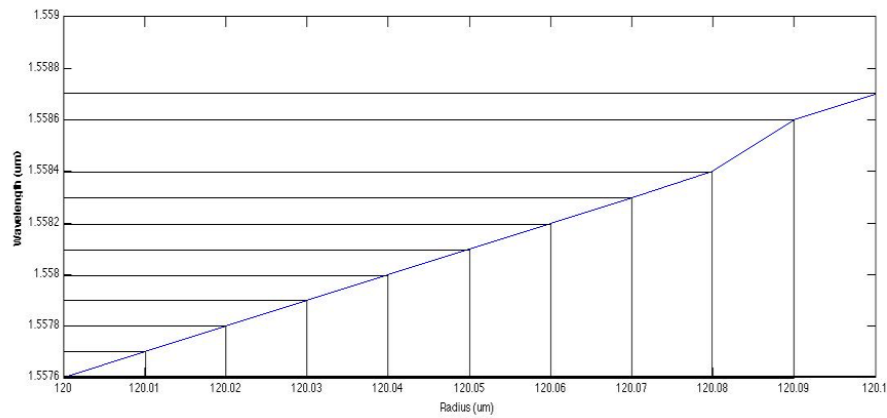
FIGURE 3.17: Transmittance as a function of distance between the waveguides.

coupling is one of the main processes towards a proper operation for any given optical resonator. In this manner, it is interesting to come up with some of the engineering decisions such as the distance between the straight and circular waveguide. During the modeling step as well as fabrication process, it should be very careful to spend sufficient time and energy.

Some tests are performed about the distance between the waveguides and how it affects the resonance spectrum. The collected data are presented. They can be utilized to index some of the records for an optimal coupling intensity between the waveguides. In order to have a better performance of an optical resonator waveguides should fulfill some of the requirements. One of the criteria is the core part should not overlap each other for both of the waveguides. Only the *cladding* parts can be overlapped. Figure 3.18 a) shows the coupling effect between the waveguides that is not in normal form to be able to establish coupling effect. This deformation is faced because the distance between the straight-form and ring-form waveguide is zero. The measurement is done in the point where they interact to each other. Thus, their core part corresponds to an overlapping to each other.

In the following graph, Figure 3.18 b) an immediate normalization in the transfer function of the resonator response is noticed. These tests are performed by slowly increasing the distance between the waveguides. It can be read from the figures all transfer functions for different distance values. In figures 3.18 c), d), e) the curves does not contain any important change since the distance between the waveguides in these cases are between $0.84\mu m$ and $0.94\mu m$. A sharper dip can be noticed in Figure 3.18 f) and it corresponds

to a distance of $1.12\mu m$. The penetration of the dip is only 0.5, or 50 %. In Figures 3.18 g) and h) can be seen the best quality of Lorentzian line shape out of all the graphs. Its intensity at resonance goes even until value of 0.15 of that amplitude. Increasing the distance between the waveguides leads to a deformation of the transfer function. This increase leads to a deformed shape of the curves and they are presented in Figures 3.18 i-3.18 k.
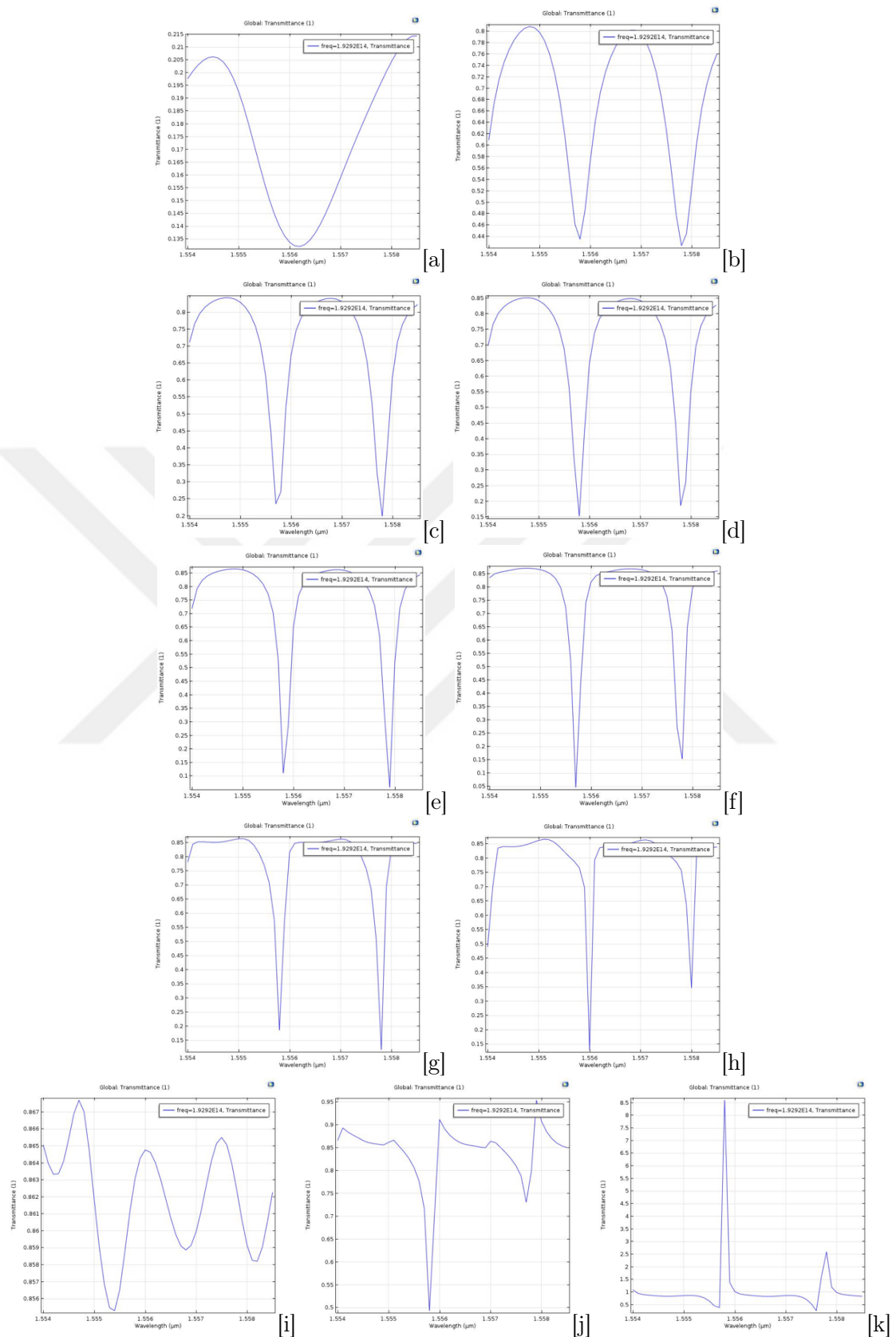
FIGURE 3.18: Resonance shift for the ring radius increasing started from $80.00\mu m$ to $80.10\mu m$.

Up to this time, all the transfer functions presented here for the resonator simulations have been implemented in a high resolution. Beside this, for illustration a lower resolution is applied in order to include more spectrum modes. Figure 3.19 shows three groups of modes that oscillate and they describe the behavior of the ring resonator. They take different form in different points and the variation of resonance amplitude can be observed.
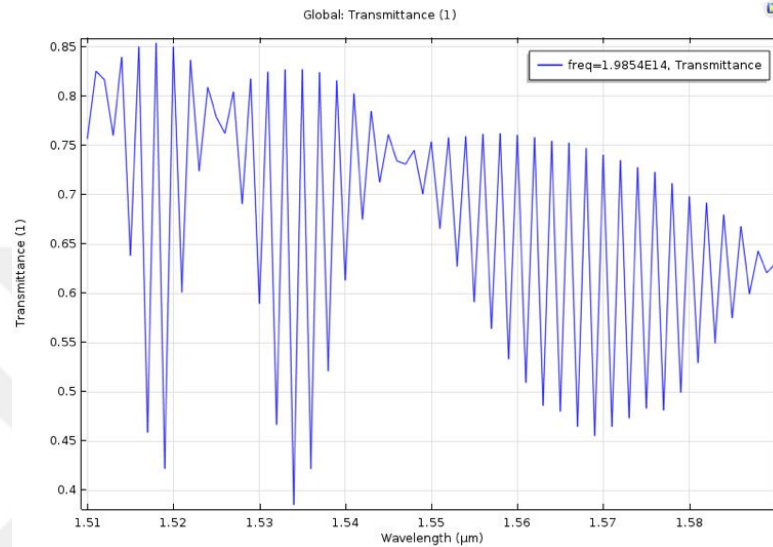
FIGURE 3.19: Simulations results for the resonator model with a lower resolution: $1.51\mu m$ to $1.60\mu m$.

In conclusion, this section presents some of the test results regarding to modeling of optical ring resonators. The aim is to reach a better performance in terms of their usage and optimization, either as scientific or researches subject.

3.4 Size and Refractive Index Variation using The Effective Medium Approximations - Yamaguchi model

This section presents the last part of the research for optical ring resonators. As it was presented on the first section of this chapter, only the thickness of the ring was changed. Similarly, here it is continued with simulations where the thickness of the ring and also the concentration of the biomolecules is changed in the same time. This extension is implemented since in real life there exists a difference between the material of the resonator and âmaterialâ of nanoparticles or biomolecules. This process was implemented through a refractive index change and the thickness change in the additional

ring. In this manner, an additional thin layer is added around the resonator which represents the biomolecules attached to the surface of the resonator and checked out the resonance spectrum. The approach for the effective refraction index was applied using Yamaguchi effect model. These simulations have included two cases: i) Titanium Dioxide Nanoparticle ($RI_{TiO_2} = 2.41$) and ii) Protein Biomolecule ($RI_{PB} = 1.45$) [17]. The effective medium approximations can be used to identify the average field that has been propagating within a homogeneous medium and was described by an effective refractive index [34]. There are many mathematical approximations for calculating the effective permittivity of a composite medium and some of them are: Yamaguchi Model [33], Maxwell-Garnett Model[35, 36], Bruggeman Model [37], etc. In our study, the model of Yamaguchi is chose to evaluate the effective refraction index (RI). This model is used also for the moaterial that will surround the layer of resonator and sensing the particles in medium, as it is more accurate for 2-Dimensional plan.

Yamaguchi Model. Since the model of Maxwell-Garnett considers that the composites that are positioned in a three-dimensional distribution of inclusions in the host medium, the mixtures with two-dimensional distributions of inclusions in any host medium can be evaluated in many times. In these cases is an approximation for this refraction index based on the work of Yamaguchi, and his model can give an excellent prediction [33]. The model relies on some of the hypothesis for similar spheroidal nanoparticles whose axis is perpendicular to any layer that is going to be analyzed. Those particles are considered as point dipoles presenting an isotropic and homogeneous in-plane distribution or systematized as a square, or hexagonal lattice [38, 39]. Figure 3.20 shows the height (h) of the composite that is equal to the diameter of nanoparticles, a is the distance between neighboring particles. The effective dielectric function of this composite layer is [37]

$$\varepsilon_{i1}^Y = \epsilon_m \left(1 + \frac{N\frac{V}{h}\alpha}{1 - \alpha\frac{VN}{4\alpha}} \right) \tag{3.3}$$

Where the height h of the composite equals the diameter of the nanoparticles, N represents the number of particles per surface unit; V represents volume of one single particle, and in this case is the in-line plane polarization of the dipoles is equivalent to

$$\alpha = \frac{V(\epsilon - \epsilon_d)}{\epsilon_d + \frac{1}{3}(\epsilon - \epsilon_d)} \tag{3.4}$$
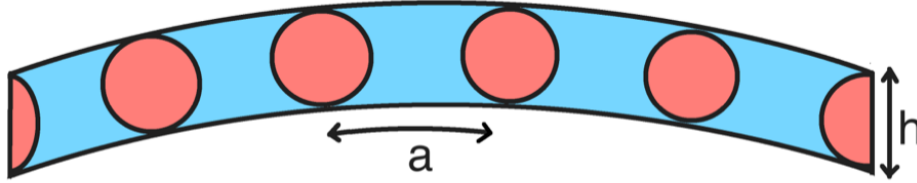
FIGURE 3.20: Mixture with spherical particles distributed in the host medium layer with a configuration in two dimensions.

Ever since the effective optical index of the composite is known by using the numerical models that were presented above, the optical properties such as absorption can be compute. After this, we will discuss the optical properties influenced by the concentration of some of the nanoparticles and Plasmon coupling.
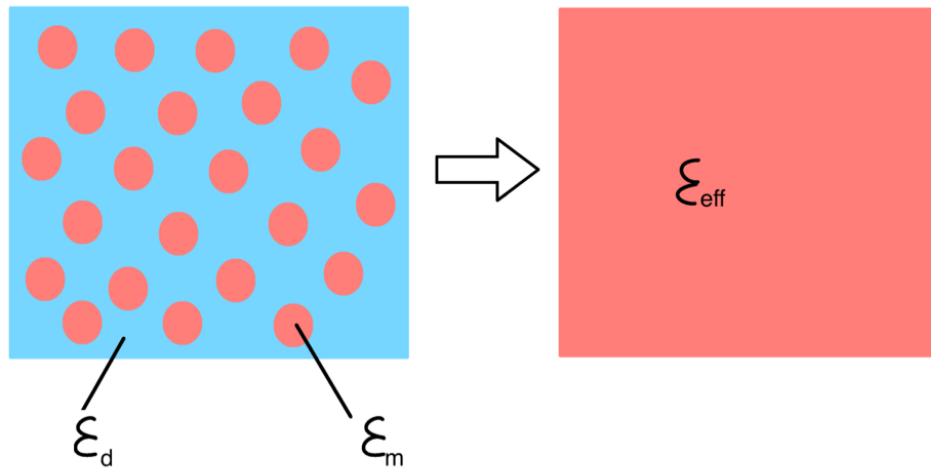
FIGURE 3.21: Yamaguchi model for the 2-Dimensional Effective Medium.

Since this work is going eventually to lead in further levels in optimization and realization of a real physical device, it is decided to work with dimensions and refractive index that correspond to the mimicked nanoparticles.

Previous parts were talking about changing only the size of the layer that was modeled to be around the ring. Now, it will be moved this in a more advance level by putting this study in morphologic changes: size and refraction index, at the same time.

The first step in modeling process is to simulate the optical response of nanoparticles embedded in the medium that surrounds the space of micro-resonator. Therefore, the focus is to calculate the response spectrum of the sample to implement it in the built model, and then to monitor how it will affect that spectrum in the end of process. After the size and refraction index of the layer are changed, probably resonator qualitatively will not behave same anymore. Simulations are performed with finite element method and Yamaguchi model approximation for effective refractive index is used.

Based on [17], values of refractive index are used for some of the nanoparticles and biomolecules that are listed. In this part of the study, effects for two nanoparticles are analyzed: Titanium Dioxide nanoparticle and Protein biomolecule. Both og these elements are considered as "dead" materials in order to come up with the engineering results for their sensing effects and the study to be more practical.

Titanium Dioxide Nanoparticle. This nanoparticle is becoming part of all our everyday lives. It can be found in a wide range of consumer goods and products of daily usage, such as cosmetics, paints, dyes and varnishes, textiles, paper and plastics, food, drugs, and even paving stones. 4.68 Million tons of titanium dioxide have been produced worldwide in 2009 and 1,5 million tons per year are produced in the European Union alone [40]. These are some characteristics that have made Titanium Dioxide nanoparticles very useful nanomaterials for academic researches, or especially for medical and industrial products.

In this way, Titanium Dioxide nanoparticles were used to characterize the interaction with the optical ring resonator model. The layer is modeled around the ring and Yamaguchi model has been chosen to obtain the effective refraction index (R_{eff}). Based on [17] refraction index for Titanium Dioxide nanoparticle is $n_{TiO_2} = 2.41$. It is assumed that the shape of these particles are spherical and the amount of those are positioned in a medium with refraction index of 1.33, and a distance between nanoparticles of $a = 20nm$. Radius of nanoparticles for the first case: $R_{NP} = 5nm$ and a height of layer: $h = 10nm$, applying to the effective dielectric function

$$\varepsilon_{eff}^{Y} = \varepsilon_m(1 + \frac{N\frac{V}{h}\alpha}{1 - \alpha\frac{VN}{4\alpha}}.) \qquad (3.5)$$

It has an effective refraction index of $n_{eff} = 7.99$, and black colored component is the corresponding response curve in Figure 3.22.

For the second case, $R_{NP} = 10nm$, $h = 20nm$ and separated distance between neighboring particle: $a = 30nm$, it was obtained an effective refraction index: $n_{eff} = 7.23$. Violet is the corresponding curve in Figure 3.22. Therefore, the size of nanoparticle is $R_{NP} = 20nm$.

The third case consists of $R_{NP} = 15nm$, a layer height of $h = 30nm$ and distance between neighboring particle $a = 30nm$, is obtained an effective refraction index:$n_{eff} = 6.95$. Brown colored is the corresponding curve in Figure 3.22.

The fourth case consists of $R_{NP} = 20nm$, a layer height of $h = 40$ and distance between neighboring particle $a = 50nm$, is obtained an effective refraction index $n_{eff} = 6.81$. Yellow colored is the corresponding curve in Figure 3.22.

The fifth case consists of $R_{NP} = 25nm$, a layer height of $h = 50$ and distance between neighboring particle is $a = 60nm$, is obtained an effective refraction index of $n_{eff} = 6.73$. Blue colored is the corresponding curve in Figure 3.22.

The sixth case consists of $R_{NP} = 30nm$, a layer height of $h = 60$ and distance between neighboring particle is $a = 70nm$, is obtained an effective refraction index of $n_{eff} = 6.67$. Green colored is the corresponding curve in Figure 3.22.

The seventh case consists of $R_{NP} = 35nm$, a layer height of $h = 70$ and distance between neighboring particle is $a = 80nm$, is obtained an effective refraction index of $n_{eff} = 6.63$. Pink colored is the corresponding curve in Figure 3.22.

The eighth case consists of $R_{NP} = 40nm$, a layer height of $h = 80$ and distance between neighboring particle $a = 90nm$, is obtained an effective refraction index of $n_{eff} = 6.60$. Orange colored is the corresponding curve in Figure 3.22.

The ninth case consists of $R_{NP} = 45nm$, a layer height of $h = 90$ and distance between neighboring particle $a = 100nm$, is obtained an effective refraction index $n_{eff} = 6.57$. Green (dark) colored is the corresponding curve in Figure 3.22.

The tenth case consists of $R_{NP} = 50nm$, a layer height of $h = 100$ and distance between neighboring particle $a = 110nm$, is obtained an effective refraction index of $n_{eff} = 6.55$. Blue (dark) colored is the corresponding curve in Figure 3.22.
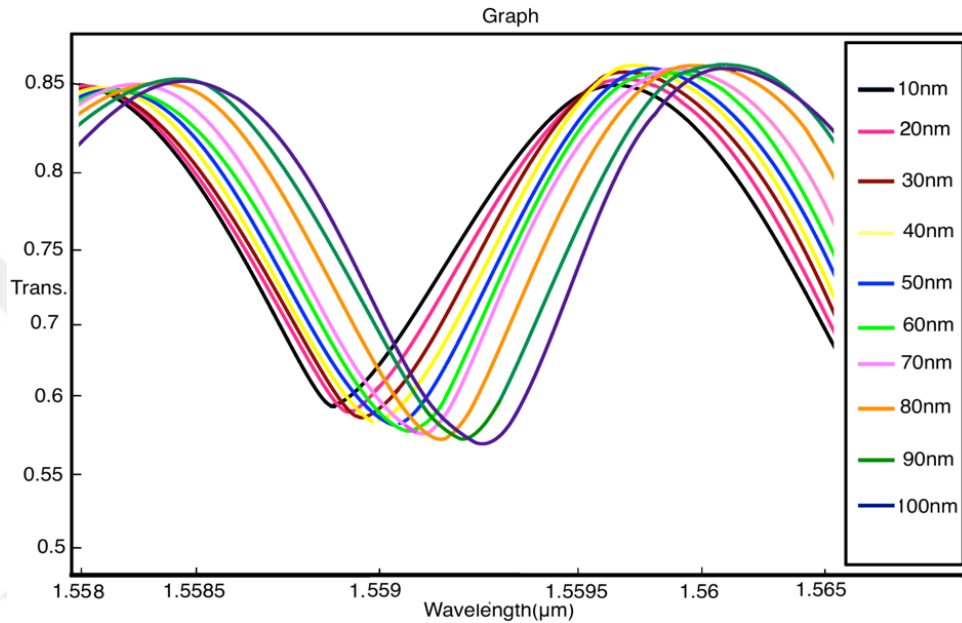

FIGURE 3.22: Resonance shift for Titanium Dioxide Nanoparticle-TiO_2-NP.

Based on this figure, it can be concluded that there exists a resonance shift for a size as low as $10nm$, $20nm$ or $30nm$. By increasing the thickness of the layer slowly is increased the value of the shift and also the dip amplitude of the resonance is enhanced. For instance, comparing 10 nm to 100 nm, an obvious difference between them exists.

Figure 3.23 shows the values variation as function of the thickness layer size. This case is for the Titanium Dioxide nanoparticle that is bound around the resonator. This graph is deduced as a different method to present the measurements from Figure 3.22. For 10 nm particle size it has been a shift of 0.05 nm from zero value. For a 50 nm particle size it has a shift of 0.175 nm, and for 100 nm particle size it has a shift of 0.3 nm. Therefore, the total shift for the size between $10nm$ to 100 nm is in the range of 0.05 nm and 0.3 nm, respectively.
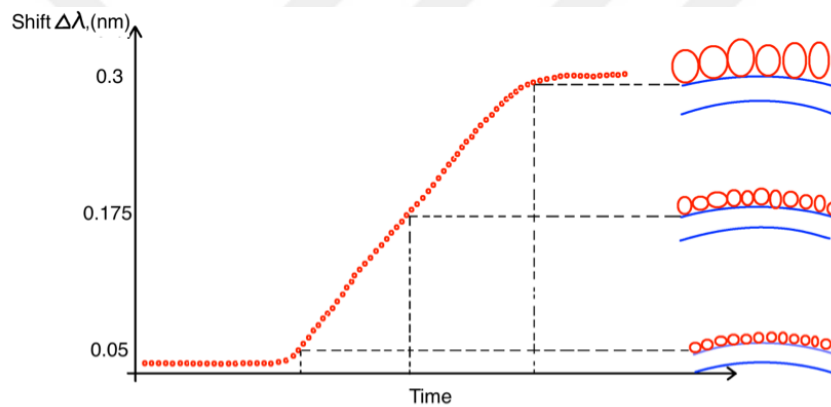

FIGURE 3.23: Resonance shift for Titanium Dioxide Nanoparticle used to describe the size of the attached particles.

Protein Molecule. Protein is a type of molecule that is a fundamental building element of every living organism. They are expressed in different ways and are structural building blocks within every organism. They execute many duties inside of the organism relating to a certain aspects of transportation of a living body. Additionally, they are crucial factors for immune system in a living organism [41].

This was an introduction-like for protein molecules, however we are interested in their physical and especially their interactions with light as physical object. Therefore, to give the model another application it has been studied for their properties and based on the reference [17], refraction index for these "materials" are n = 1.45.

Also here is the same procedure as the previous one and it will be analyzed for every single step each.

In first case we have, $R_{mol} = 5nm$, the height of the layer $h = 10nm$ and separate distance center to center between neighboring particle is $a = 20nm$, it is obtained an effective refraction index $n_{eff} = 4.8$. The black colored component (line) is the corresponding curve in Figure 3.24. Therefore, the diameter of this supposed molecule is $10nm$.

For second case, $R_{mol} = 10nm$ and $h = 20nm$ separated distance between neighboring particle $a = 30nm$, it is obtained an effective refraction index $n_{eff} = 4.35$. Brown colored component is the corresponding curve in Figure 3.24. Therefore, the size of biomolecule is $20nm$.

The third case consists of $R_{mol} = 15nm$, a layer height of $h = 30nm$ and distance between neighboring particle $a = 40nm$, is obtained an effective refraction index $n_{eff} = 4.18$. Red colored component is the corresponding curve in Figure 3.24.

The fourth case consists of $R_{mol} = 20nm$, a layer height of $h = 40nm$ and distance between neighboring particle $a = 50nm$, obtained an effective refraction index $n_{eff} = 4.10$. Green colored component is the corresponding curve in Figure 3.24.

The fifth case consists of $R_{mol} = 25nm$, a layer height of $h = 50nm$ and distance between neighboring particle $a = 60nm$, is obtained an effective refraction index $n_{eff} = 4.04$. Blue colored component is the corresponding curve in Figure 3.24.

The sixth case consists of $R_{mol} = 30nm$, a layer height of $h = 60nm$ and distance between neighboring particle $a = 70nm$, obtained an effective refraction index $n_{eff} = 4.01$. Violet colored component is the corresponding curve in Figure 3.24.

The seventh case consists of $R_{mol} = 35nm$, a layer height of $h = 70nm$and distance between neighboring particle $a = 80nm$, obtained an effective refraction index $n_{eff} = 3.98$. Orange colored component is the corresponding curve in Figure 3.24.

The eighth case consists of $R_{mol} = 40nm$, a layer height of $h = 80nm$ and distance between neighboring particle $a = 90nm$, obtained an effective refraction index $n_{eff} = 3.97$. Green (dark) colored line is the corresponding curve in Figure 3.24.

The ninth case consists of $R_{mol} = 45nm$, a layer height of $h = 90nm$ and distance between neighboring particle $a = 100nm$, obtained an effective refraction index $n_{eff} = 3.95$. Gold colored component is the corresponding curve in Figure 3.24.

The tenth case consists of $R_{mol} = 50nm$, a layer height of $h = 100nm$ and distance between neighboring particle $a = 110nm$. An effective refraction index $n_{eff} = 3.94$ is obtained. Grey component is the corresponding curve in Figure 3.24.
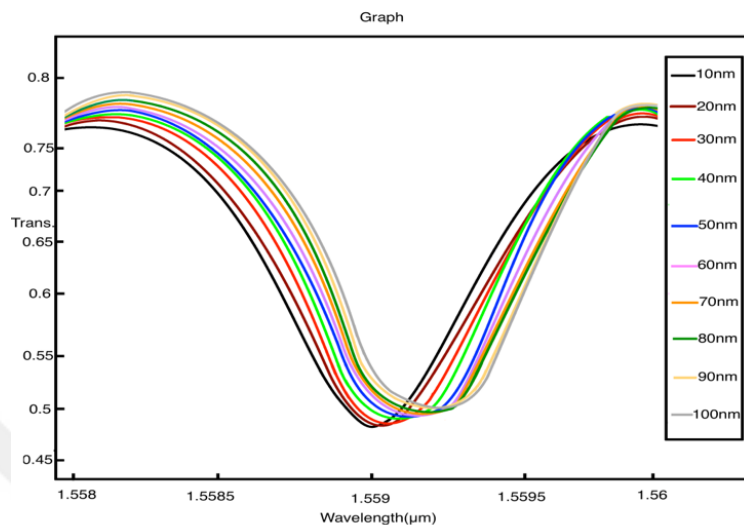
FIGURE 3.24: Simulations for Protein Moleculeresonance shift.

These shift variations are quantified and plotted in Figure 3.25. In this graph, those variations contains slightly higher shift comparing to the graph of Titanium Dioxide Nanoparticle.

FIGURE 3.25: Resonance shift for the Protein Molecule.

In this section, all the information are presented to conduct some of the test results regarding to modeling of optical ring resonators. The aim is to reach a better performance for these devices in terms of usage and optimization, either as scientific or researches subject.

Chapter 4

Conclusion and Future Work

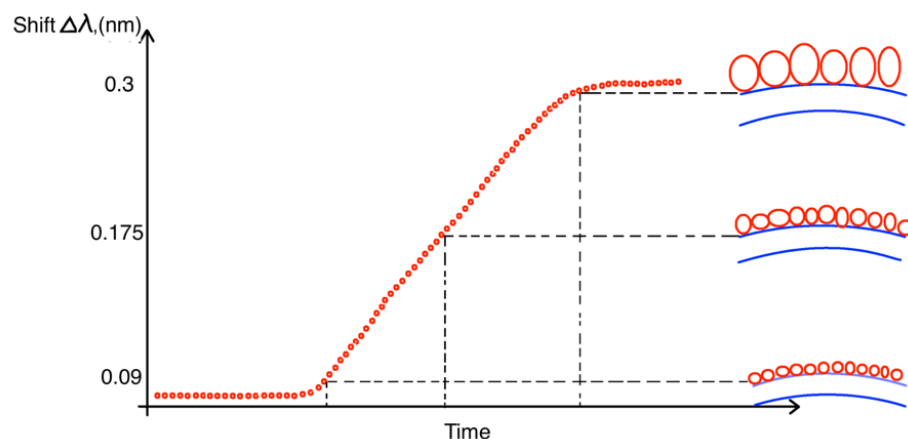This study has been conducted with the aim to exploring the characteristics of microring resonator as label-free platform towards biomolecules and nanoparticles detection. A computation-based model with the finite element method has been developed. This model is performed to simulate the optical ring resonator in order to solve its equations. Nanoparticles are approached as nanosphere and when they are aligned with each other they are supposed to create a structure layer-like around the ring. In the simulations, an increment of 10 nm for the ring radius between 83.00 μm and 83.10 μm was applied. A linear correlation between increasing the ring radius and the red shift of the wavelength resonance is found. The linear decrease between increasing the size of the ring and decreasing FSR was observed. The last part of this thesis shows the modification of the layer in different size as and more important with different refraction index, simultaneously. This morphological change is realized to mimic the material for titanium dioxide nanoparticle and protein biomolecule. The size of nanoparticles is mimicked by thickness of the layer, which is performed until 100 μm thickness, and the corresponding graph of resonance spectrum was introduced.

Moreover, the distance between nanoparticles and their number in an assembly have been demonstrated to affect their transient dynamics, approximated with 2-D Yamaguchi Model. The closer the particles are to each other the larger are in number. The results that are revealed in this work can be very promising for industrial and biomedical applications. A large number of projects are devoted recently to such developments that are being carried by using nanostructures as optically-controlled.

Optical microresonators have shown a great potential for commercialization with a huge superior ultra-high sensitivity, even for single nanoparticle detection. Another advantage of micro-resonators consists of the effective way of delivering sample material in to the sensing place, which lead to a high reduction of clinical analysis time. Resonators used as biosensors are foreseen to have a bright future in clinical diagnostics since they are label-free analytic detectors and can be integrated on a chip-scaled devices.

The future aim consists of developing this model in further steps and potentially to proceed in real-world applications such as sensing tool prototype. However, in this project much more work is still to be done . One of them is to modify the layer by applying different properties of material in order to mimic different biomolecules that may be attached from the sample. Furthermore, an original idea consists of to consider this platform as Microelectromechanical (MEMS) system. This step can be implemented in the future terms.

It would be implemented by applying an electrical field around the ring, and by adjusting the intensity of electrical field in order to manually change the diameter of the ring. After this procedure, the resonator would not behave the same anymore. In this way, it would be an interesting research to check how it would react.

Bibliography

[1] B. Kaltenboeck and C. M. Wang. Advances in real-time PCR: Application to clinical laboratory diagnostics. *Elsevier Academic Press Inc*, 40: pages 219–259, 2005.

[2] M. Dufva. Fabrication of high quality microarrays. *Biomol. Eng.*, 22: pages 173–184, 2005.

[3] D. G. Rabus. *Integrated Ring Resonators: The compendium.* Springer, 2007.

[4] N. X. Tan. Micro and nanophotonic structures in the visible near to infrared spectral for optical devices. Master's thesis, Barcelona, Spain, 2013.

[5] J. Liu. *Photonic devices.* Cambridge University Press, 2009.

[6] Wikipedia. Wikipedia - photonics. URL `https://en.wikipedia.org/wiki/Photonics`.

[7] J. Heebner, R. Grover, and T. Ibrahim. *Optical Microresonators - Theory, Fabrication, and Application.* Springer, 2008.

[8] P. Feron. Waveguide-coupled algaas/gaas microcavity ring and disk resonators with high finesse and 21.6 nm free spectral range. *Annales de la Fondation Louis de Broglie*, 29: pages 317–329, 2004.

[9] F. Vollmer, S. Arnold, and D. Keng. Single virus detection from the reactive shift of a whispering gallery-mode. *Proceedings of the National Academy of Sciences of the United States of America*, 105: pages 20701–20704, 2008.

[10] F. Vollmer and S. Arnold. Whispering- gallery-mode biosensing: label-free detection down to single molecules. *Optics Letters*, 5: pages 591–596, 2008.

[11] Wikipedia. Wikipedia Photonics. URL `https://en.wikipedia.org/wiki/Optical_ring_resonators`.

[12] S. Daud, S.M. Idrus, and J. Ali. *Simulation of Optical Soliton in Micro- and Nanoring Resonator Systems.* Springer, 2015.

[13] L. Stokes, M. Chodow, and H. Shaq. All-single-mode fiber resonator. *Optics Letters*, 7: pages 219–259, 1984.

[14] D. Y. Chu, M. K. Chin, N. J. Sauer, Z. Xu, T. Y. Chang, and S. T. Ho. 1.5 μm ingaas/inalgaas quantum-well microdisk lasers. *IEEE Photonics Technology Letters*, 5: pages 219–259, 1993.

[15] D. Rafizadeh, J. P. Zhang, S. C. Hagness, A. Taflove, K. A. Stair, S. T. Ho, and R. C. Tiberio. Waveguide-coupled algaas/gaas microcavity ring and disk resonators with high finesse and 21.6 nm free spectral range. *IEEE Photonics Technology Letters*, 22: pages 1244–1246, 1997.

[16] P. Absil. *Microring resonators for wavelength division multiplexing and integrated photonics applications.* PhD thesis, University of Maryland, College Park, 2000.

[17] Malvern. Refractive index of gold and other nanoparticles. URL `http://www.materials-talks.com/blog/2014/08/05/faq-how-important-are-refractive-index-absorption-for-nanoparticles/`.

[18] A. Ramachandran, S. Wang, J. Clarke, S. Ja, D. Goad, L. Wald, E. Flood, E. Knobbe, J. Hryniewicz, S. Chu, D. Gill, W. Chen, D. King, and B. Little. A universal biosensing platform based on optical micro-ring resonators. *Biosensors and Bioelectronics*, 23: pages 939–944, 2008.

[19] P. Yeh. *Optical Waves in Layered Media.* Wiley, New York, 1988.

[20] A.N. Oraevsky. Whispering-gallery waves. *Quantum Electron*, 32(4): pages 377–400, 2001.

[21] Jenikya. Jenikya blog - st. paul cathedral picture. URL `http://jenikya.com/blog/pa-wedding-30.jpg`.

[22] Online Electronics Forum. Oef - web site. URL `http://www.radio-electronics.com/info/formulae/q-quality-factor/basics-tutorial.php`.

[23] L. Tobing and P. Dumon. *Fundamental Principles of Operation and Notes on Fabrication of Photonic Microresonators.* Springer, United States, 2010.

[24] K.J. Vahala. Optical microcavities. *Nature*, 424: pages 839–846, 2003.

[25] M. Gomilsek. Whispering gallery mode. *Seminar, University of Ljublana*, 2011.

[26] E. Franchimon. *Modelling circular optical microresonators using whispering gallery modes*. PhD thesis, University of Twente, Enschede, Netherlands, 2010.

[27] M. Gorodetsky, A. Pryamikov, and V. Ilchenko. Rayleigh scattering in high-q microspheres. *The Optical Society of America*, 17: pages 1051–1057, 2000.

[28] T. Kippenberg. *Nonlinear Optics in Ultra-High-Q Whispering-Gallery Optical Microcavities*. PhD thesis, California Institute of Technology, California, US, 2004.

[29] Y. Ido. Reduced lasing threshold in thiophene/phenylene co-oligomer crystalline microdisks. *Applied Physics Express*, 3: pages 2702, 2010.

[30] H. Zhu, M. Snyder, and C. Opin. Protein chip technology. *Chem. Biol.*, 7: pages 55–63, 2003.

[31] M. Baaske and F. Vollmer. Optical resonator biosensors: Molecular diagnostic and nanoparticle detection on an integrated platform. *ChemPhysChem*, 13: pages 427–436, 2012.

[32] F. Ahmeti and K. Teker. A model for an optical ring resonator towards nanoparticle detection. *Tech Connect World 2017*, 3: pages 254–257, 2017.

[33] T. Yamaguchi, S. Yoshida, and A. Kinbara. Effective-medium theory for finite-size aggregates. *Thin Solid Films*, 21: pages 173–187, 1974.

[34] C. Guerin, P. Mallet, and A. Sentenac. Effective-medium theory for finite-size aggregates. *J. Opt. Soc. Am. A*, 23: pages 349–358, 2006.

[35] J. Garnett. Colors in metal glasses and in metallic films. *Physical and Engineering Sciences*, 203: pages 385–420, 1904.

[36] J. Garnett. Colors in metal glasses, in metallic films, and in metallic solutions. ii. *Transactions of the Royal Society A: Mathematical, Physical and Engineering Sciences*, 205: pages 337–288, 1906.

[37] D. Bruggeman. The calculation of various physical constants of heterogeneous substances. the dielectric constants and conductivities of mixtures composed of isotropic substances. *Ann. Phys.*, 24: pages 636–664, 1935.

[38] X. Wang. *Photo-induced ultrafast optical and thermal responses of gold nanoparticles*. PhD thesis, LâUniversite Pierre Et Marie Curie, Paris, France, 2013.

[39] J. Toudert, D. Babonneau, L. Simonot, S. Camelio, and T. Girardeau. Quantitative modeling of the surface plasmon resonances of metal nanoclusters sandwiched between dielectric layers: the influence of nanocluster size, shape and organization. *Nanotechnology*, 19(33): pages 125709, 2008.

[40] Data and knowledge on nanomaterials. Titanium dioxide - material information - web site. URL `http://nanopartikel.info/en/nanoinfo/materials/titanium-dioxide`.

[41] Study. Study website. URL `http://study.com/academy/lesson/protein-molecules-functions-structure-examples.html`.